nature cell biology

Article

https://doi.org/10.1038/s41556-024-01511-x

Plasma membrane curvature regulates the formation of contacts with the endoplasmic reticulum

Received: 20 November 2023

Accepted: 19 August 2024

Published online: 17 September 2024

Check for updates

Yang Yang[1,2], Luis A. Valencia[1,2], Chih-Hao Lu[1,2], Melissa L. Nakamoto[1,2], Ching-Ting Tsai[1,2], Chun Liu[3,10], Huaxiao Yang[3,11], Wei Zhang[1,2], Zeinab Jahed[1,12], Wan-Ru Lee[4], Francesca Santoro[5,6,7], Jen Liou[4], Joseph C. Wu[3,8,9] & Bianxiao Cui[1,2]

Contact sites between the endoplasmic reticulum (ER) and plasma membrane (PM) play a crucial role in governing calcium regulation and lipid homeostasis. Despite their significance, the factors regulating their spatial distribution on the PM remain elusive. Inspired by observations in cardiomyocytes, where ER–PM contact sites concentrate on tubular PM invaginations known as transverse tubules, we hypothesize that PM curvature plays a role in ER–PM contact formation. Through precise control of PM invaginations, we show that PM curvatures locally induce the formation of ER–PM contacts in cardiomyocytes. Intriguingly, the junctophilin family of ER–PM tethering proteins, specifically expressed in excitable cells, is the key player in this process, whereas the ubiquitously expressed extended synaptotagmin-2 does not show a preference for PM curvature. At the mechanistic level, we find that the low-complexity region (LCR) and membrane occupation and recognition nexus (MORN) motifs of junctophilins can bind independently to the PM, but both the LCR and MORN motifs are required for targeting PM curvatures. By examining the junctophilin interactome, we identify a family of curvature-sensing proteins—Eps15 homology domain-containing proteins—that interact with the MORN_LCR motifs and facilitate the preferential tethering of junctophilins to curved PM. These findings highlight the pivotal role of PM curvature in the formation of ER–PM contacts in cardiomyocytes and unveil a mechanism for the spatial regulation of ER–PM contacts through PM curvature modulation.

In eukaryotic cells, the endoplasmic reticulum (ER) plays a central role in membrane protein synthesis, lipid production and calcium storage. At certain locations, the ER membrane and plasma membrane (PM) are brought into close proximity by ER–PM tethering proteins, typically within a range of 10–30 nm (refs. 1,2), to form ER–PM contacts. These contact sites play pivotal roles in lipid exchange, calcium signalling and phospholipid signalling[3–5]. Disruptions in ER–PM contacts have been associated with a variety of diseases, including cardiovascular and neurodegenerative diseases[6–10].

Notably, ER–PM contact sites are not uniformly distributed on the PM. For example, in pancreatic acinar cells[11] and hepatocytes[12], ER–PM contacts are enriched at the basal membrane but are nearly absent from the apical region. T cells preferentially form ER–PM contacts at immunological synapses[13], whereas neurons form dense ER–PM contacts in dendrites and sparse contacts in axons[14,15]. The spatial organization of ER–PM contacts is believed to function as a mechanism regulating local calcium influx and subcellular responses. However, the precise mechanisms governing such spatial organization remain to be fully elucidated.

A full list of affiliations appears at the end of the paper. e-mail: bcui@stanford.edu

An intriguing example of non-uniform ER–PM contact sites is in striated muscle cells. In these cells, ER–PM contacts preferentially form on tubular PM invaginations known as transverse tubules (T-tubules)[16–18], which penetrate into the cytoplasmic domain and establish extensive contacts with the ER, referred to as dyad junctions in cardiomyocytes. Early studies showed that ER–PM contacts are five times more likely to form on the sarcolemma (namely the PM in muscle cells) at the T-tubules compared with the sarcolemma in other areas of mammalian ventricular cardiomyocytes[17]. Dyad junctions in cardiomyocytes are crucial for regulating the rapid influx of calcium and mediating excitation–contraction coupling. Loss of T-tubules is accompanied by disorganized dyad junctions, disrupted calcium responses, increased susceptibility to arrhythmia and impaired contractile function of cardiomyocytes in patients with heart diseases[19]. However, the molecular mechanism underlying the enrichment of ER–PM contacts at T-tubules remains largely underexplored.

The curvature of the PM is emerging as a pivotal regulator of cellular activities. Cells respond to PM curvatures through curvature-sensing proteins, which have distinct structures for sensing and influencing membrane bending[20]. Recent studies have revealed that PM curvatures actively participate in a diverse range of cellular processes, including ion channel activity[21], membrane trafficking[22], signal transduction[23] and mechanotransduction[24]. In this Article, we hypothesize that PM morphology can regulate the formation of ER–PM contacts through local PM curvatures and curvature-sensing proteins. Using vertical nanostructures to control PM curvatures, we found that in cardiomyocytes PM curvature promotes the site-specific formation of ER–PM contacts—a process mediated by junctophilin-2 (JPH2), an ER–PM tethering protein. Furthermore, we find that JPH-mediated ER–PM contacts also exhibit a preference for PM curvature in non-muscle cells. In contrast, extended synaptotagmins (E-Syts)—another family of ER–PM tethering proteins—do not exhibit a preference for PM curvature. Mechanistically, our investigation identified Eps15 homology domain-containing proteins (EHDs) as a crucial family of curvature-sensing proteins that interact with JPHs and convey the preference for PM curvature.

Results

Nanopillar-induced PM invaginations recruit dyad components

To assess the role of PM curvature in dyad junction formation, we used human induced pluripotent stem cell-derived cardiomyocytes (iPSC-CMs). These immature iPSC-CMs lack T-tubule structures, which develop postnatally. T-tubules typically have diameters ranging from 20–450 nm, pitches (the lateral distance between neighbouring tubules) of 1.8–2.5 μm and depths of 1–9 μm (ref. 25). To mimic T-tubule shapes, we fabricated vertical quartz nanopillars measuring 200–300 nm in diameter, 2.5 μm in pitch and 2 μm in height (Fig. 1a). When cells are cultured on nanopillars, their PM wraps around the nanopillars and forms inward membrane tubules (Fig. 1b). In this Article, we refer to the ER in non-muscle cells and the sarcoplasmic reticulum in cardiomyocytes both as ER and the PM in non-muscle cells and the sarcolemma in cardiomyocytes both as PM.

To determine whether nanopillar-induced PM invaginations trigger local ER–PM contact formation in iPSC-CMs, we immunostained JPH2—a transmembrane ER protein that tethers ER membranes to the PM at contact sites in cardiomyocytes. We also co-stained α-actinin (a marker for *z*-lines to reflect the integrity of sarcomeres) and transfected the cells with green fluorescent protein (GFP)-tagged Sec61β (GFP-Sec61β) to visualize the general ER distribution. In cells cultured on flat areas, α-actinin showed a characteristic well-ordered sarcomere pattern, whereas JPH2 appeared as numerous small puncta widely distributed in cells (Fig. 1c). In contrast, cells cultured on nanopillar areas showed strong JPH2 accumulation at regularly spaced nanopillars, unlike GFP-Sec61β, which did not show accumulation on nanopillars (Fig. 1d). The α-actinin staining showed that *z*-lines were not spatially correlated with nanopillars and mostly avoided them. Bright-field images, PM markers and additional representative examples of JPH2, α-actinin and GFP-Sec61β co-imaging are included in Extended Data Fig. 1a.

Averaged images of over ~3,000 nanopillars clearly illustrated that JPH2 preferentially accumulated at nanopillar locations, whereas α-actinin and GFP-Sec61β slightly avoided nanopillars. Averaged intensity profiles along the yellow horizontal lines in Fig. 1e confirmed this observation (Fig. 1f). Quantifying the fluorescence intensity ratio at nanopillars (the area within the circular magenta mask) versus between nanopillars (the area inside the yellow donut mask) revealed a consistent ratio of ~2 for JPH2 and ~0.9 for both α-actinin and GFP-Sec61β (Fig. 1g), indicating a preferential accumulation of JPH2 at nanopillar-induced PM curvatures.

To investigate whether ER–PM contacts formed at nanopillar-induced PM invaginations incorporate crucial components of functional dyad junctions, we immunostained ryanodine receptor 2 (RyR2; an ER calcium release channel) and Cav1.2 (a subunit of the L-type calcium channel (LTCC)) on the PM. RyR2 and LTCC are known to colocalize at dyad junctions to facilitate voltage-induced calcium influx and subsequent stored calcium release during cardiac excitation–contraction coupling[26]. We found that, similar to JPH2, RyR2 accumulated prominently at nanopillar-induced PM invaginations, whereas GFP-Sec61β did not (Fig. 1h). Co-staining of RyR2 with calreticulin (an ER lumen protein) as an additional general ER marker besides GFP-Sec61β showed a similar effect (Extended Data Fig. 1b). Although all cells showed preferential accumulation of JPH2 and RyR2 at nanopillars, only some cells showed Cav1.2 accumulation (Fig. 1h). This variability in

Fig. 1 | Nanopillar-induced PM invaginations recruit dyad components in cardiomyocytes. a, SEM images of nanopillars. Scale bars, 1 μm (left) and 500 nm (right). **b**, Left: Schematic of a T-tubule system in a cardiomyocyte. Middle: ER–PM contacts at T-tubules. Right: Nanopillar-induced membrane invaginations. **c**,**d**, Co-immunostaining of JPH2 (green) and α-actinin (red) in iPSC-CMs expressing GFP-Sec61β (magenta) on flat (**c**) and nanopillar (**d**) areas. Bottom: Enlarged views of the regions shown in the yellow boxes. Scale bars, 10 μm (top) and 2.5 μm (bottom). **e**, Average fluorescence signals of GFP-Sec61β, JPH2 and α-actinin over ~3,000 nanopillars; $n = 18$, 21 and 21 cells for GFP-Sec61β, JPH2 and α-actinin, respectively. Scale bars, 2.5 μm. **f**, Average intensity plots along the horizontal yellow line shown in **e**, normalized by the intensity of the region between two nanopillars. The error bars represent s.d. among values from individual cells. **g**, Ratio of the fluorescence intensity at nanopillars (magenta mask) to that at non-pillar areas (yellow mask). Scale bar, 2.5 μm; $n = 21$, 10, 11, 18 and 21 cells for JPH2, RyR2, Cav1.2, Sec61β and α-actinin, respectively. The data are presented as means ± s.d. $^{****}P < 0.0001$; $^{**}P = 0.0067$. NS, not significant ($P > 0.9999$). **h**, Co-immunostaining of RyR2 (green) and Cav1.2 (red) in iPSC-CMs expressing GFP-Sec61β (magenta) on nanopillars. A filled arrowhead points to cells with a clear Cav1.2 signal, whereas an open arrowhead points to cells with minimal Cav1.2. Scale bars, 10 μm (top) and 2.5 μm (bottom). **i**, Average fluorescence signals of RyR2 and Cav1.2 over ~1,200 nanopillars; $n = 10$ and 11 cells for RyR2 and Cav1.2, respectively. Scale bars, 2.5 μm. **j**, SEM images of nanobars. Scale bars, 5 μm (top) and 2 μm (bottom). **k**, Representative images of iPSC-CMs expressing BFP-CAAX immunostained with JPH2, RyR2 and Cav1.2 on nanobars. Middle: Enlarged views of the regions shown in the yellow boxes. Bottom: The average fluorescence signals of all nanobars from multiple cells; $n = 23$, 23, 23 and 11 cells for BFP-CAAX, JPH2, RyR2 and Cav1.2, respectively. Scale bars, 10 μm (top) and 2.5 μm (middle and bottom). **l**, Quantification of the fluorescence intensity ratio at the nanobar ends (magenta mask) versus the sides (green mask). Scale bar, 2.5 μm. The cell numbers were as in **k**. The data are presented as means ± s.d. $^{****}P < 0.0001$; $^{*}P = 0.0277$. All the experiments were replicated independently three times with similar results. Statistical significance in **g** and **l** was determined by Kruskal–Wallis test corrected with Dunn's multiple comparisons test. Source numerical data are available Source data.

https://doi.org/10.1038/s41556-024-01511-x

Cav1.2 may be due to the immaturity and heterogeneity of iPSC-CMs[27] and the relatively late developmental expression of Cav1.2 (ref. 28). Averaged images of RyR2 and Cav1.2 (Fig. 1i) and quantitative analyses in cells with high Cav1.2 expression (Fig. 1g) demonstrated their preferential accumulation at nanopillar-induced PM invaginations, indicating the formation of functional ER–PM contacts at PM curvatures. In addition, we also examined iPSC-CMs from a commercial source (iCells) and primary rat embryonic cardiomyocytes. Immunostaining of RyR and JPH2 in these cells also showed strong accumulations at nanopillar locations (Extended Data Fig. 1c).

We engineered vertical nanobars to induce both curved and flat PMs on the same nanostructure (Fig. 1j). These nanobars, with dimensions of 2 µm height, 200–300 nm width, 5 µm length and 10 µm pitch, induce high PM curvatures at their vertical ends and horizontal top and flat membranes along their sidewalls, serving as internal controls. When imaging at the mid-height of the nanobars, the PM curvature is

https://doi.org/10.1038/s41556-024-01511-x

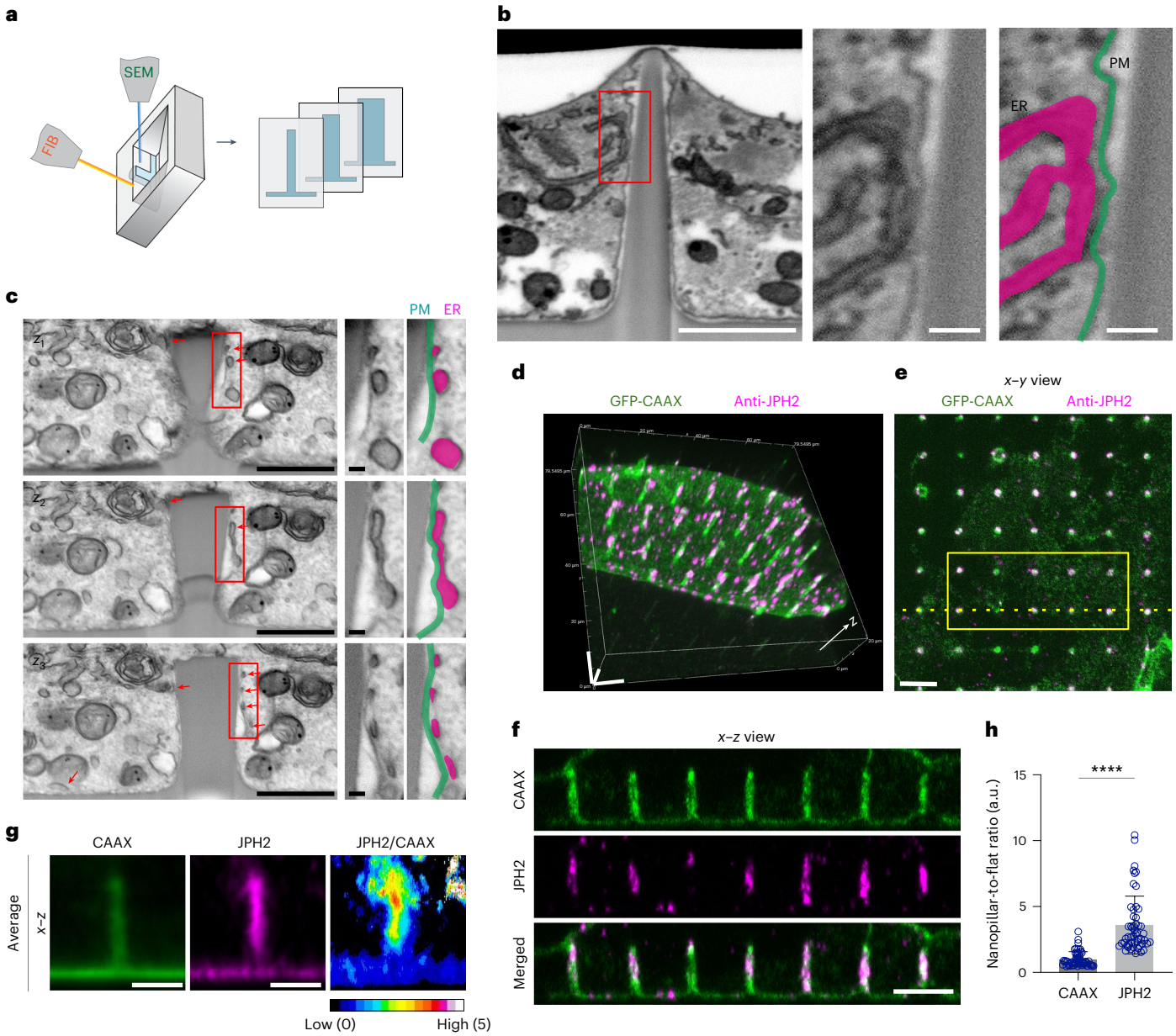

Fig. 2 | Nanopillar-induced membrane invaginations promote the local formation of ER–PM contacts in cardiomyocytes. a, Schematic of using FIB-SEM to examine the cell–nanopillar interface. **b**, Left: A FIB-SEM image of the interface between an iPSC-CM and a nanopillar. This image is black–white inverted for clarity. Scale bar, 1 µm. Middle: An enlarged view of the region shown in the red box. Scale bar, 100 nm. Right: As for the middle image, but with the PM (green) and ER (magenta) highlighted in pseudo colours. **c**, Left: Three different FIB-SEM sections of an HL-1 cardiomyocyte on the same nanopillar. The red arrows indicate ER–PM contact sites. Scale bars, 1 µm. Middle and right: Enlarged views as in **b**. Scale bars, 100 nm. **d**, ExM imaging of an iPSC-CM cultured on nanopillars. GFP-CAAX is shown in green and anti-JPH2 is shown in magenta. Scale bars, 10 µm (in each dimension). **e**, An *x*–*y* image focused on the middle height of nanopillars using an expansion microscope. Scale bar, 10 µm. **f**, The *x*–*z* view along the yellow dashed line shown in **e**. The *z* dimension was scaled by the ratio between the *z*-step size and *x*–*y* pixel size to exhibit *x* and *z* at the same dimensional scale. Scale bar, 10 µm. **g**, An averaged *x*–*z* image of the ten pillars shown in the yellow box in **e**. The intensities were normalized by the inter-pillar intensities on flat membranes for both CAAX and JPH2 channels and then displayed at the same scale. Right: The ratiometric image is the ratio between JPH2 and CAAX channels. Scale bars, 5 µm. **h**, Quantifications of the nanopillar-to-flat intensity ratios for GFP-CAAX and JPH2, normalized by the average intensity ratio for GFP-CAAX. Each dot represents the averaged ratio for a region of nanopillars inside a cell (typically five or six pillars); $n = 52$ regions from 15 cells for each probe. The data are presented as means ± s.d. ****$P < 0.0001$. The experiments in **b** and **c** were replicated independently twice with similar results and the other experiments were replicated independently three times with similar results. Statistical significance in **h** was determined by two-tailed Mann–Whitney test. Source numerical data are available Source data.

pronounced at the nanobar ends. Staining results showed that JPH2, RyR2 and Cav1.2 preferentially accumulated at the bar ends, confirming their localization to membrane curvatures. In comparison, the expressed PM marker BFP-CAAX (blue fluorescent protein fused to a prenylation motif) uniformly wrapped around the nanobars, displaying no curvature preference (Fig. 1k,l).

PM invaginations promote ER–PM contact formation

To directly visualize ER–PM contacts, we used focused ion beam scanning electron microscopy (FIB-SEM) to image membrane interfaces at nanopillar locations (Fig. 2a). Figure 2b shows a typical SEM image of the cardiomyocyte–nanopillar interface, with a clear ER–PM contact on the nanopillar's left side. FIB-SEM enables sequential FIB milling

for volumetric SEM imaging. We obtained a series of 36 SEM images to visualize ER–PM contacts in a cardiomyocyte interfaced with a nanopillar (Supplementary Video 1). Multiple ER–PM contacts were observed on the PM surrounding a single nanopillar (Fig. 2c). Serial images show interconnected ER tubules and sheets with large ER–PM contact patches evolving into smaller, distinct patches in different cross-section images (red arrows in Fig. 2c). From the 36 SEM images, the ER–PM contact density on the curved PM surrounding nanopillars was ~3.6 times that on the flat PM (Extended Data Fig. 2). The FIB-SEM measurements suggest that ER–PM contacts preferentially form on curved PM.

The FIB-SEM imaging method is valuable but limited in throughput, restricting quantitative measurements. To address this, we used expansion microscopy (ExM)[29,30] to examine more nanopillars and cells, enhancing the data robustness (Fig. 2d and Supplementary Video 2). Confocal imaging of the expanded sample provided high-resolution visualization of JPH2 puncta on the PM, both at the nanopillar sites and the flat areas. In x–y plane images, both JPH2 and the PM marker GFP-CAAX exhibited considerably higher intensities at the nanopillar locations due to the vertical projection effect of the PM wrapping around the nanopillars (Fig. 2e). The x–z plane images revealed a clear preferential accumulation of JPH2 signals, compared with GFP-CAAX, on nanopillars than at flat areas between nanopillars (Fig. 2f).

To assess JPH2's preference for PM curvature, we averaged x–z plane images of a row of nanopillars and the surrounding flat areas, normalizing the intensity of JPH2 against that of GFP-CAAX (Fig. 2g). The normalized image clearly showed higher JPH2 density at curved PMs surrounding nanopillars compared with the flat area (Fig. 2g). Quantitative analysis revealed that the pillar-to-flat ratio for JPH2 was 3.8 ± 1.4 times higher than that of CAAX (Fig. 2h). Therefore, JPH2 is significantly enriched on curved PMs surrounding nanopillars, confirming that ER–PM contacts preferentially form on curved PMs in iPSC-CMs.

JPHs, but not E-Syt2, exhibit preferences for PM curvatures

T-tubules are only present in mature striated muscle cells. To examine whether JPH2-mediated ER–PM contacts also prefer PM curvatures in non-muscle cells, we transfected mCherry-JPH2 into U2OS cells, a human osteosarcoma cell line. For U2OS studies, we employed smaller nanobars with 1 µm height, 200 nm width, 2 µm length and 5 µm pitch (Fig. 3a) to induce membrane curvatures in U2OS cells, as these cells are more readily deformed than CMs.

In U2OS cells, mCherry-JPH2 showed selective enrichment at nanobar ends, indicating a preference for PM curvature (Fig. 3b). The ER marker GFP-Sec61β and the PM marker BFP-CAAX did not accumulate at the nanobar ends (Fig. 3b). Although JPH2 is not normally expressed in U2OS cells, its homologues JPH3 and JPH4 are, according to the RNA sequencing database[31]. When GFP-JPH2, GFP-JPH3 or GFP-JPH4 were transiently expressed in U2OS cells, all three displayed a pronounced preference for PM curvature at nanobar ends (Fig. 3c). The averaged images showed that GFP-CAAX exhibited even PM wrapping around the nanobars, whereas GFP-JPH2, GFP-JPH3 or GFP-JPH4 revealed dumbbell distributions featuring pronounced protein accumulations at nanobar ends (Fig. 3d). The end-to-side intensity ratios for JPH2, JPH3 and JPH4 were significantly higher than that of CAAX, which was close to 1 (Fig. 3e), indicating a strong preference of JPHs for PM curvature. We noticed that GFP-JPH2 exhibited a higher ER network population compared with GFP-JPH3 and GFP-JPH4, probably because JPH3 and JPH4 are endogenously expressed in U2OS cells, but JPH2 is not. For subsequent investigations in U2OS cells, we selected JPH3 as the representative JPH for its lower intracellular fluorescence background.

To determine whether the curvature preference is unique to JPH or a shared feature of ER–PM tethers, we examined E-Syt2—a ubiquitously expressed ER–PM tethering protein[32]. Unlike JPHs, GFP-E-Syt2 often avoided the nanobar ends and located along the sidewalls (Fig. 3f). Co-transfected mCherry-Sec61β did not accumulate on the nanobars and BFP-CAAX evenly wrapped around the nanobars (Fig. 3f). Averaged images showed GFP-E-Syt2 accumulation along the sidewalls, in sharp contrast with GFP-JPH3's accumulation at the nanobar ends (Fig. 3g). This behaviour was consistent in HeLa and HEK cells (Fig. 3g and Extended Data Fig. 3a). Quantifying the end-to-side ratios in the three cell lines confirmed that JPH3 preferentially binds to curved PMs at nanobar ends, whereas E-Syt2 shows no such preference (Fig. 3h).

We investigated whether GFP-JPH3 retains its curvature preference in artificially induced ER–PM contacts using a dimerization-dependent fluorescent protein (ddFP) technology[33]. ddFP involves the reversible binding of two dark components, GB and RA, that form a fluorescent dimer when in close proximity. We constructed GB-CAAX to target the PM and RA-Sec61β to target the ER. At ER–PM contacts, the two components bind and become fluorescent (Extended Data Fig. 3b). Overexpression of GB-CAAX and RA-Sec61β induced extensive ER–PM contacts (Extended Data Fig. 3c), probably due to the relatively low dissociation rate between RA and GB[33]. Interestingly, although GFP-JPH3 entirely colocalized with ddFP in contact patches on flat areas, JPH3 showed a stronger preference for nanobar ends than ddFP (Extended Data Fig. 3d), confirming JPH3's preference for curved PMs.

Finally, to visualize ER–PM contacts in U2OS cells without overexpressing tethering proteins, we used the ER–PM marker GFP-MAPPER (membrane-attached peripheral ER), which is incorporated into existing ER–PM contacts with minimum perturbations[34]. GFP-MAPPER exhibited a curvature preference with an end-to-side ratio of 1.65 ± 0.26, suggesting that endogenous ER–PM contacts in U2OS cells preferentially form on curved PM (Fig. 3i,j). When coexpressed with mCherry-JPH3, MAPPER accumulated at the nanobar ends. In contrast, when coexpressed with E-Syt2, MAPPER colocalized with E-Syt2 without obvious curvature preference, confirming that JPH3-mediated, but not E-Syt2-mediated, ER–PM contacts preferentially form on curved PMs (Extended Data Fig. 3e).

Active STIM1 and ORAI1 locate to ER–PM contacts formed on curved PM

Store-operated calcium entry is crucial for intracellular calcium homeostasis and relies on stromal interaction molecule 1 (STIM1) and calcium release-activated calcium channel protein 1 (ORAI1). STIM1, an ER-resident calcium sensor, oligomerizes and translocates to ER–PM contact sites when the ER calcium decreases[35,36]. There, STIM1 interacts with the PM-resident ORAI1 calcium channel to facilitate store-operated calcium entry[37–40]. STIM1 has been recognized to primarily localize to pre-existing ER–PM contacts upon activation[35]. We examined whether STIM1 and ORAI1 incorporate into ER–PM contact sites on curved PM upon calcium depletion. U2OS cells were used for their ease of transfection and clear localization of ER–PM contacts to PM curvatures.

In the resting state, GFP-JPH3 formed ER–PM contacts at nanobar ends, whereas mCherry-STIM1 mainly localized within the ER network with minimal localization to nanobars (Fig. 4a). After a 5 min treatment with 2 µM thapsigargin (Tg) to deplete the ER calcium, mCherry-STIM1 clustered at the nanobar ends and colocalized with GFP-JPH3 (Fig. 4a). ORAI1 was uniformly distributed around the nanobars in the resting state (Fig. 4b) and redistributed to ER–PM contact sites located at the nanobar ends colocalizing with STIM1 after Tg treatment (Fig. 4b and Supplementary Video 3). ORAI1 and STIM1 exhibited similar clustering kinetics comparing the curved PM and the flat PM (Fig. 4c). On curved PMs, STIM1 and ORAI1 displayed similar accumulation kinetics (Fig. 4d). Averaged nanobar images (Fig. 4e) and end-to-side ratio quantification (Fig. 4f) confirmed that STIM1 and ORAI1 translocated to the nanobar ends upon calcium depletion.

Synergistic roles of the low-complexity region and membrane occupation and recognition nexus motifs in PM and curvature targeting

JPHs have eight conserved membrane occupation and recognition nexus (MORN) motifs, a long low-complexity region (LCR) joining the

https://doi.org/10.1038/s41556-024-01511-x

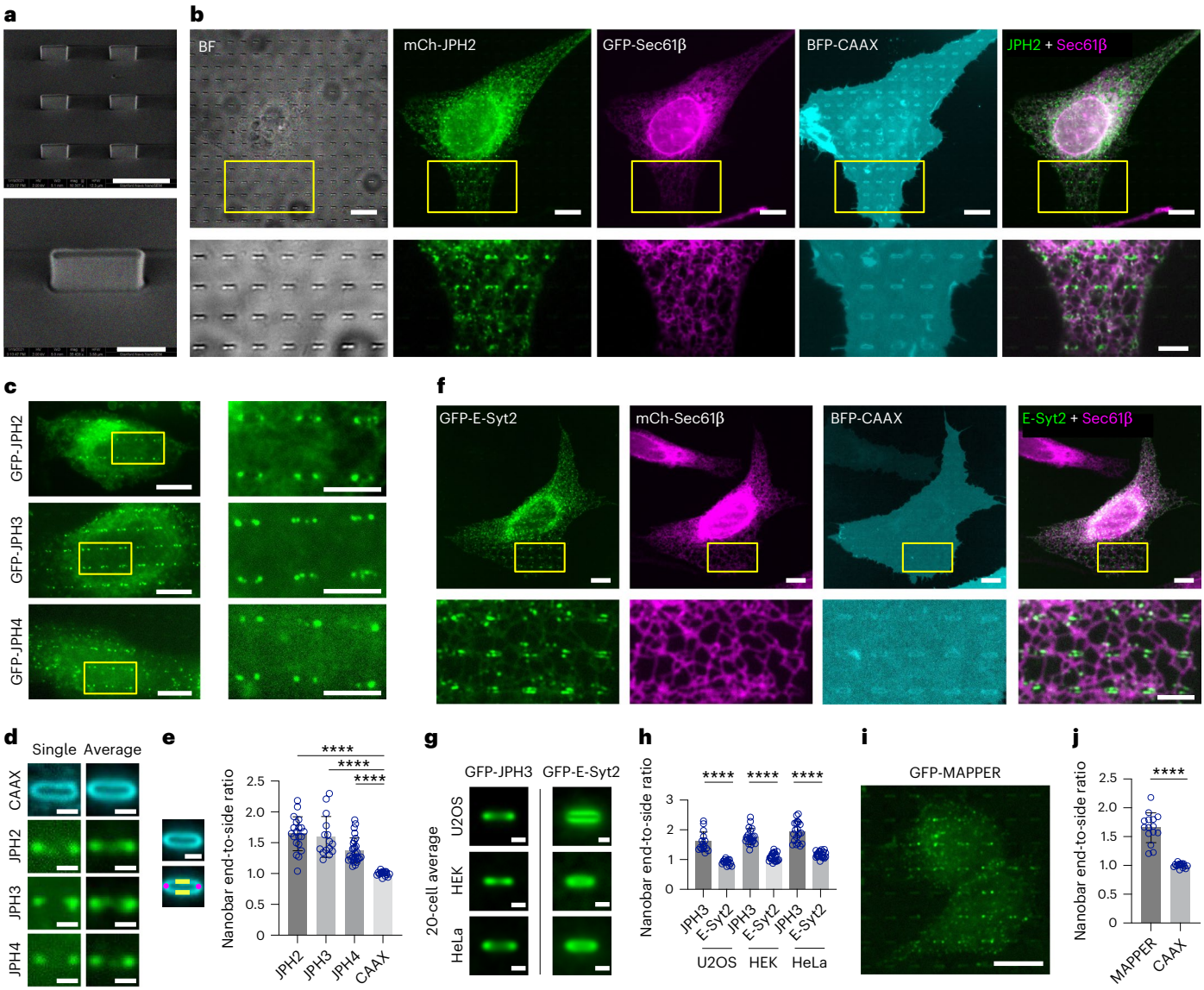

Fig. 3 | JPH tethering proteins, but not E-Syt2, exhibit a strong preference for PM curvatures. a, SEM images of nanobars. Scale bars, 4 µm (top) and 1 µm (bottom). **b**, Bright-field (BF) images of U2OS cells and immunofluorescence images of U2OS cells coexpressing mCherry-JPH2 (mCh-JPH2; green), GFP-Sec61β (magenta) and BFP-CAAX (cyan). mCh-JPH2 preferentially accumulates at the ends of nanobars. Bottom: Enlarged images of the regions marked by a yellow box. Right: Merged JPH2 and Sec61β images. Scale bars, 10 µm (top) and 5 µm (bottom). **c**, Representative images of GFP-JPH2, GFP-JPH3 and GFP-JPH4 preferentially accumulating at nanobar ends. Right: Enlarged images of the regions marked by yellow boxes. Scale bars, 10 µm (left) and 5 µm (right). **d**, Enlarged single and average nanobar (averaged within a single cell) images of the cells shown in **c**. Scale bars, 1 µm. **e**, Quantification of the nanobar end-to-side ratios calculated using average intensity at the bar ends (magenta mask) divided by that at the bar sides (yellow mask). Scale bars, 1 µm. Each dot represents the average value of a single cell; $n = 20$, 15, 27 and 15 cells for JPH2, JPH3, JPH4 and CAAX, respectively. $^{****}P < 0.0001$. **f**, U2OS cells coexpressing GFP-E-Syt2 (green), mCherry-Sec61β (magenta) and BFP-CAAX (cyan). GFP-E-Syt2 does not preferentially accumulate at nanobar ends. Bottom: Enlarged images of the regions marked by yellow boxes. Right: Merged image of GFP-E-Syt2 and mCherry-Sec61β. Scale bars, 10 µm (top) and 5 µm (bottom). **g**, Average nanobar images of GFP-JPH3 and GFP-E-Syt2 singly expressed in U2OS, HEK and HeLa cells; $n = 20$ cells for each probe in each cell line. Scale bars, 1 µm. **h**, Quantifications of the end-to-side intensity ratios for GFP-JPH3 or GFP-E-Syt2 in U2OS cells, HEK293T cells or HeLa cells; $n = 20$ cells per condition. $^{****}P < 0.0001$. **i**, U2OS cells expressing GFP-MAPPER on nanobars. Scale bar, 10 µm. **j**, Quantifications of the nanobar end-to-side ratios for GFP-MAPPER and GFP-CAAX; $n = 15$ cells per probe. $^{****}P < 0.0001$. All the experiments were replicated independently three times with similar results. The data in **e**, **h** and **j** are presented as means ± s.d. Statistical significance was determined by one-way Brown–Forsythe and Welch analysis of variance (ANOVA) tests (**e** and **h**) or two-tailed Welch's *t*-test (**j**). Source numerical data are available Source data.

segment between MORN6 and MORN7, an α-helix domain (αHelix) and an ER transmembrane domain (Fig. 5a). Some studies suggest that MORN repeats tether the PM by binding to phospholipids[41,42], whereas others indicate weak or no phospholipid interactions for MORN motifs[43,44]. The LCR's function is unclear but it may act as a steric hindrance decreasing the binding affinity between JPH and the LTCC[44]. We engineered JPH3 truncations and mutations to identify the motifs responsible for JPH3's PM binding and curvature sensing (Fig. 5a).

We found that the Δ8MORNΔLCR construct, which lacks JPH3's amino (N)-terminal eight MORN domains and LCR, completely lost its PM targeting capability (Fig. 5b). This construct colocalizes with Sec61β at the intracellular ER network, consistent with previous studies

https://doi.org/10.1038/s41556-024-01511-x

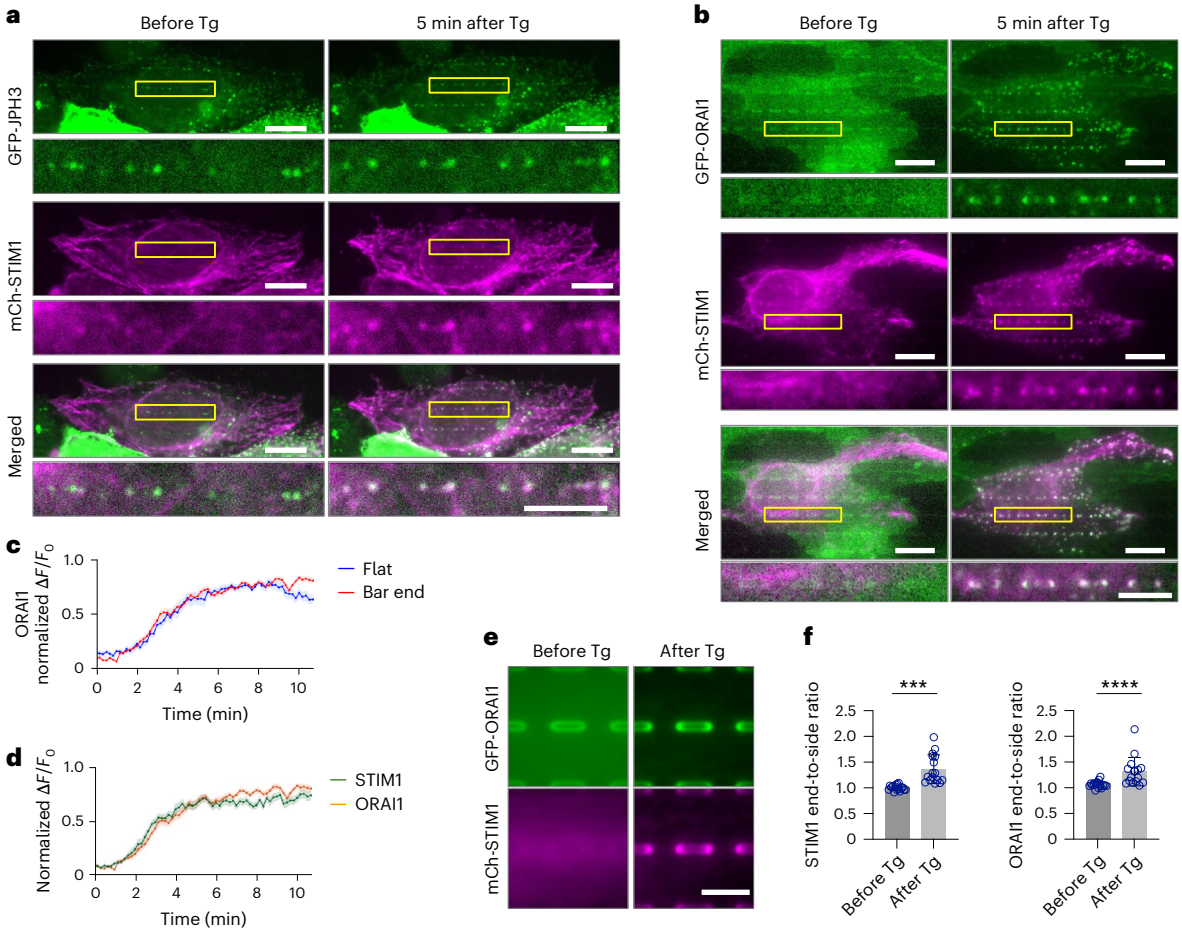

Fig. 4 | STIM1 and ORAI1 are incorporated into ER–PM contacts formed on curved PM following calcium depletion. a,**b**, U2OS cells co-transfected with mCherry-STIM1 and GFP-JPH3 (**a**) or GFP-ORAI1 (**b**) before and 5–10 min after 10 μM Tg treatment. Tg treatment induced accumulations of mCherry-STIM1 and GFP-ORAI1 at nanobar ends. Enlarged views of the regions shown in yellow boxes are displayed at the bottom of each image. Scale bars, 10 μm (whole cell images) and 5 μm (magnified images). **c**, Relative time-dependent increases (normalized $\Delta F/F_0$) of ORAI1 cluster intensities at the bar end and on the flat area in cells co-transfected with mCherry-STIM1 and GFP-ORAI1 upon Tg treatment. The intensities of regions of 0.85 × 0.85 μm^2 at ORAI1 clusters formed at nanobar ends or on flat areas were calculated. Representative averaging of normalized $\Delta F/F_0$ traces are shown. Normalized $\Delta F/F_0$ traces were normalized to their plateau value before averaging. $n = 21$ regions from seven cells. The shaded error bars represent s.e.m. **d**, Relative time-dependent increases of STIM1 and ORAI1 cluster intensities at bar ends upon Tg treatment. Average intensities of STIM1 and ORAI1 were calculated from the same cells and regions as in **c**. Normalized $\Delta F/F_0$ traces were normalized to their plateau value before averaging to compare between different probes. The shaded error bars represent s.e.m. **e**, Averaged nanobar images for mCh-STIM1 and GFP-ORAI1 before and after Tg treatment; $n = 16$ cells per condition. Scale bar, 2.5 μm. **f**, Quantifications of the end-to-side ratios for mCh-STIM1 and GFP-ORAI1 before and after Tg treatment; $n = 16$ cells per condition. The data are presented as means ± s.d. ***$P = 0.0001$; ****$P < 0.0001$. All the experiments were replicated independently three times with similar results. Statistical significance was determined by two-tailed Welch's t-test (STIM1 in **f**) or two-tailed Mann–Whitney test (ORAI1 in **f**). Source numerical data are available Source data.

showing that the N-terminal fragment is crucial for JPH3's ER–PM tethering function[41].

To determine whether MORN motifs are crucial for PM tethering, we constructed an Δ8MORN variant by linking LCR to the N terminus of the Δ8MORNΔLCR construct. Surprisingly, unlike Δ8MORNΔLCR, Δ8MORN formed discrete ER–PM contacts (Fig. 5c), suggesting that LCR binds directly to the PM or to the components in ER–PM contacts. To test LCR's direct PM binding, we fused LCR to GFP (GFP-LCR), which showed strong PM localization and nuclear localization (Fig. 5d), demonstrating LCR's high PM affinity. We examined the LCR sequence in the four human *JPH* genes and identified a conserved polybasic sequence in LCR (Extended Data Fig. 4a). Mutations leading to the substitution of six cationic amino acids (p.Lys210Ala, p.Lys211Ala, p.Lys212Ala, p.Lys224Ala, p.Arg226Ala and p.Lys227Ala (LCR-KRtoA)) abolished GFP-LCR's PM and nuclear localization (Fig. 5e), demonstrating that the cationic charges are responsible in this process. To further examine whether the high affinity of LCR for the PM is sufficient to induce ER–PM contact formation, we directly linked LCR to the ER transmembrane domain (LCR-TM). Unlike the homogenous distribution of LCR on the PM, LCR-TM was spatially constrained by the ER network and displayed large and discrete patches at ER–PM contact sites (Fig. 5f), confirming the capability of LCR-TM to tether the ER to the PM. These results demonstrate that the LCR in JPH3 tethers the PM, probably through electrostatic interactions between its polybasic sequence and negatively charged phospholipids.

Next, to investigate the role of MORN motifs in PM targeting, we generated an ΔLCR variant (Fig. 5a). Surprisingly, ΔLCR was efficiently incorporated into ER–PM contacts (Fig. 5g), suggesting that MORN motifs either directly or indirectly bind to the PM. To confirm this, we constructed GFP-8MORN, lacking LCR. In U2OS cells, GFP-8MORN appeared diffusive and cytosolic without clear nanobar wrapping, but showed membrane ruffle-like features at cell edges, indicating weak PM binding (Fig. 5h). To investigate the potential enhancement of structural stability of MORN by the α-helical domain[44], we generated

GFP-8MORN-αHelix, which was mostly nuclear localized and displayed clear membrane ruffles at the cell periphery, indicating PM affinity (Fig. 5i). To better visualize PM localization, we used confocal microscopy to image LCR, 8MORN and 8MORN-αHelix. Confocal imaging showed that the PM affinity of 8MORN-αHelix was stronger than that of 8MORN, probably due to the structural stability provided by the αHelix, but less than that of LCR (Fig. 5j).

Although Δ8MORN, ΔLCR and LCR could bind the PM, they did not show obvious curvature preference (Fig. 5c,d,g,k). It is worth noting that expression levels affect the behaviour of ER–PM tethers: low expression leads constructs to be sorted into existing contacts, whereas high expression induces ER–PM contact patches larger than the normal range. Therefore, we used intermediate expressions for quantitative measurements to assess the curvature preference of specific constructs in ER–PM contacts (see Methods for details). Additionally, constructs without the transmembrane domain have higher cytosolic background, resulting in lower ratios compared with those with the transmembrane domain. Therefore, we compared constructs with and without the transmembrane domain separately (Fig. 5l). Quantitative analysis of the nanobar end-to-side ratios showed that GFP-Δ8MORN, GFP-ΔLCR and GFP-LCR-TM had decreased curvature preferences compared with full-length JPH3 (Fig. 5l). GFP-LCR and GFP-8MORN-αHelix showed no obvious curvature preference compared with the membrane marker CAAX (Fig. 5l). Thus, although LCR or MORN motifs alone can bind the PM, neither is sufficient for curvature sensing. Additionally, to also determine the potential role of the transmembrane domain in curvature sensing, we examined the JPH3-Sec61β construct, with the transmembrane domain of JPH3 replaced with that of Sec61β. JPH3-Sec61β retained similar curvature sensing to full-length JPH3, indicating that the transmembrane domain does not influence JPH3's PM curvature preference (Fig. 5k–m).

Since neither MORN motifs nor the LCR alone is sufficient to mediate curvature sensing, we constructed GFP-8MORN_LCR and GFP-8MORN_LCR-αHelix, which include eight MORN motifs and the joining LCR, with or without the αHelix. Interestingly, both constructs exhibited PM localization and a clear preference for PM curvature at the nanobar ends (Fig. 5k,n,o). GFP-8MORN_LCR-αHelix had a more uniform PM distribution, probably due to αHelix's stabilizing effect. Quantifications showed that 8MORN_LCR and 8MORN_LCR-αHelix had significantly higher PM curvature preferences than LCR and 8MORN-αHelix (Fig. 5l). Similarly, 8MORN_LCR-αHelix of both JPH2 and JPH4 exhibited PM binding and curvature-targeting properties (Fig. 5k,l,p). These results indicate that both the 8MORN motifs and LCR are required for JPH's curvature sensing.

Pathogenic variants of JPH2, such as p.Ser101Arg, p.Tyr141His and p.Ser165Phe, have been associated with hypertrophic cardiomyopathy and impaired cellular calcium handling[45]. Our measurements revealed that both p.Ser101Arg and p.Ser101Arg exhibit significantly impaired curvature localization, with decreased nanobar end-to-side ratios compared with wild-type JPH2 (Extended Data Fig. 4b,c). However, mutation leading to p.Tyr141His did not affect JPH2's curvature sensing (Extended Data Fig. 4b,c). These findings suggest that p.Ser101Arg and p.Ser101Arg, but not p.Tyr141His, may contribute to cardiac pathology through decreased preference for PM curvature.

EHDs interact with JPHs and convey PM curvature preference

As JPHs do not harbour any known curvature-sensing domain, we hypothesized that JPHs' curvature preference arises from their interactions with other curvature-sensitive proteins. To identify such proteins, we analysed the JPH2 interactome from a published study[46]. Among more than 700 proteins, we identified seven proteins—clathrin heavy chain, EHD2, EHD4 and caveolae-associated proteins 1, 2, 3 and 4 (CAVIN1–4)—as candidates that are both PM localized and curvature sensitive (Fig. 6a and Supplementary Table 1). Of these proteins, previous research has shown that EHDs and CAVINs are curvature-sensing proteins participating in caveolae[47–51] and T-tubule formation[52–55], whereas clathrin is a crucial component of clathrin-mediated endocytosis. Clathrin preferentially accumulates at nanobar ends, as reported in a previous study[22]. We further confirmed the PM curvature sensitivity of EHD4, CAVIN1, caveolin-1 (CAV1) and CAV2 in U2OS cells using nanobar analysis (Extended Data Fig. 5a).

To determine which proteins are crucial for JPHs' curvature targeting, we used small hairpin interference RNA (shRNA) to separately knock down clathrin heavy chain, EHD1/2/4, CAVIN1 or CAV1/2 isoforms that are expressed in U2OS cells (Extended Data Fig. 5b). Although caveolins were not detected in the JPH2 interactome, we included caveolins due to their known interaction with EHDs and CAVINs and previous evidence for JPH–caveolin interactions[56–58]. Successful knockdown was confirmed by western blotting (Extended Data Fig. 5c). Knockdown of clathrin heavy chain, CAVIN1 or both CAV1 and CAV2 did not affect JPH3's preferential accumulation at the nanobar ends (Fig. 6b,c). However, triple knockdown of EHD1, 2 and 4 significantly inhibited JPH3's accumulation at nanobar ends (Fig. 6b,c). These results indicate that the EHD family is crucial for JPH3's curvature preference.

When coexpressed, different EHD isoforms, such as EHD1 and EHD4, or EHD2 and EHD4, extensively colocalize (Extended Data Fig. 5d). Because both EHD2 and EHD4 are identified in JPH's interactome and EHD4 shows a higher peptide count[46], we used EHD4 as a representative of the EHD family in our investigation. Coexpressed EHD4-mCherry and GFP-JPH3 both preferentially accumulated at nanobar ends (Extended Data Fig. 5e), indicating that EHD4 is located at JPH3-mediated contact sites at curved PMs. However, it is necessary

Fig. 5 | A conserved polybasic sequence LCR region and MORN motifs synergistically mediate the PM binding and the curvature sensing of JPH3. a, Domain structures of JPH3 and the eight engineered variants. TM, transmembrane domain. The numbers in brackets indicate amino acid positions. **b**, U2OS cells coexpressing mCherry-Sec61β with GFP-JPH3 or GFP-Δ8MORNΔLCR. Right: Enlarged views of the regions shown in the yellow boxes. **c**–**i**, Representative images of U2OS cells expressing GFP-tagged JPH3 constructs (Δ8MORN (**c**), LCR (**d**), LCR-KRtoA (**e**), LCR-TM (**f**), ΔLCR (**g**), 8MORN (**h**) and 8MORN-αHelix (**i**)) on nanobars. Left: Whole cell images. Middle: Enlarged views of the regions shown in the yellow boxes. Right: BF images of the enlarged views of the regions shown in the yellow boxes. Bottom: Enlarged view of the region shown in the red box (**h**). **j**, Representative confocal images of U2OS cells expressing GFP-LCR, mCh-8MORN or GFP-8MORN-αHelix. Top: whole cell images. Bottom: Enlarged views of the regions shown in the yellow boxes. **k**, Averaged nanobar images of cells expressing the indicated probes, displayed at the same contrast scale. Scale bars, 2.5 μm. The image areas are 10 μm × 10 μm. Cell numbers were $n = 15$ (full-length JPH3), 20 (Δ8MORNΔLCR), 9 (Δ8MORN), 20 (LCR), 16 (LCR-KRtoA), 20 (LCR-TM), 17 (JPH3-Sec61β), 8 (ΔLCR), 20 (8MORN), 20 (8MORN-αHelix), 20 (8MORN_LCR), 21 (JPH3:8MORN_LCR-αHelix), 13 (JPH2:8MORN_LCR-αHelix), 10 (JPH4:8MORN_LCR-αHelix) and 20 (CAAX). **l**, Left: Quantifications of the nanobar end-to-side ratios for constructs with the transmembrane domain (full-length JPH3, JPH3-Sec61β, Δ8MORN, LCR-TM and ΔLCR). Right: Quantifications of the nanobar end-to-side ratios for constructs without the transmembrane domain (CAAX, 8MORN-αHelix, LCR, 8MORN_LCR and 8MORN_LCR-αHelix of JPH3, JPH2 and JPH4). The cell numbers were the same as in **k**. The data are presented as means ± s.d. $^{****}P < 0.0001$; $^{***}P = 0.0002$; NS, $P = 0.2232$ (JPH3-Sec61β), $P = 0.8345$ (8MORN-αHelix) and $P = 0.1468$ (LCR). **m**–**p**, Representative images of U2OS cells expressing GFP-tagged JPH3 constructs: JPH3-Sec61β (**m**), 8MORN_LCR (**n**), 8MORN_LCR-αHelix of JPH3 (**o**) and 8MORN_LCR-αHelix of JPH2 and JPH4 (**p**) on nanobars. Left: Whole cell images. Middle: Enlarged views of the regions shown in the yellow boxes. Right: BF images of the regions shown in the yellow boxes. Scale bars, 10 μm (whole cell) and 5 μm (enlarged images), unless otherwise stated. All the experiments were replicated independently three times with similar results. Statistical significance in **l** (both left and right) was determined by one-way Brown–Forsythe and Welch ANOVA test. Source numerical data are available Source data.

https://doi.org/10.1038/s41556-024-01511-x

to point out that EHD4 and JPH3 only partially colocalized, probably due to their involvement in other independent cellular processes.

In addition to U2OS cells, we also confirmed the curvature preference of EHDs and their roles in ER–PM contact formation in cardiomyocytes. Immunofluorescence staining of EHD2 and EHD4 in both iPSC-CMs and rat embryonic CMs showed prominent enrichment at curved PM regions surrounding nanopillars (Extended Data Fig. 5f). Quantification of EHD4's nanobar end-to-side ratio in iPSC-CMs confirmed this curvature preference (Extended Data Fig. 5g). Similar to what was observed in U2OS cells, triple knockdown of EHD1, EHD2 and EHD4 in iPSC-CMs significantly decreased the end-to-side ratio of JPH2 (Extended Data Fig. 5h).

We further confirmed the role of EHDs with pharmaceutical perturbations. Cholesterol extraction using methyl-β-cyclodextrin

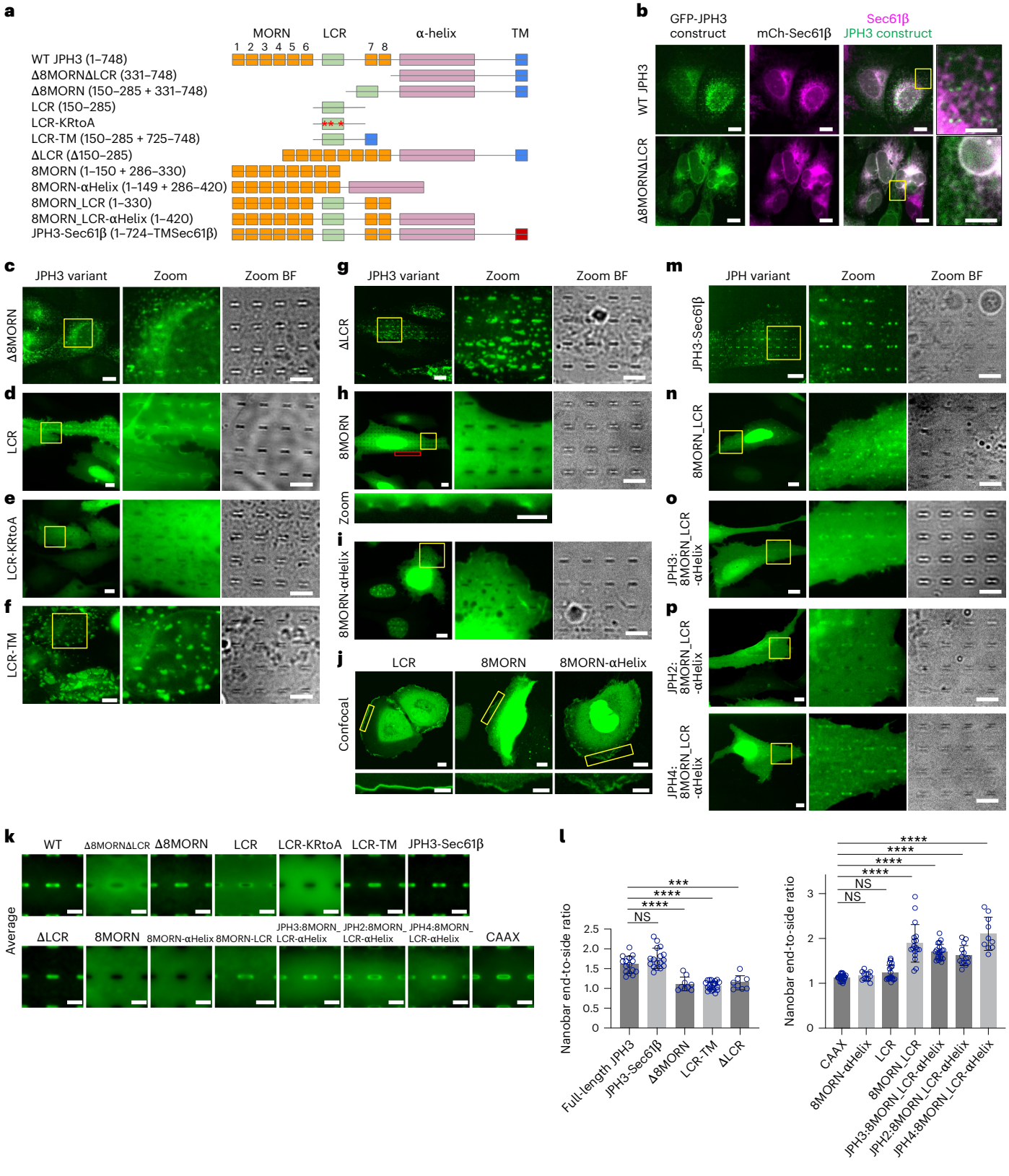

substantially disrupts EHD protein localization[59]. GFP-EHD4 exhibited a drastic loss of PM curvature preference after methyl-β-cyclodextrin treatment (Extended Data Fig. 6a). Cholesterol depletion led to a profound relocalization of GFP-JPH3 from the nanobar ends to the sides (Fig. 6d). The averaged nanobar image shifted from a dumbbell shape to two parallel lines alongside the walls of the nanobars and the nanobar end-to-side ratio decreased from 1.60 to 0.95 (Fig. 6e). These results further support the role of EHD proteins in JPH3's PM curvature preference.

Given the 8MORN_LCR domain's preference for PM curvature, we hypothesized that EHDs interact with this JPH3 region. To test this, we separately coexpressed 8MORN_LCR, 8MORN_LCR-αHelix, 8MORN-αHelix or LCR with EHD4 in U2OS cells. EHD4 formed puncta or tubular structures on the PM (Fig. 6f), which are typical of curvature-sensing proteins and agree with previous studies[47,48]. Both 8MORN_LCR and 8MORN_LCR-αHelix strongly colocalized with EHD4 in these punctate structures, whereas 8MORN-αHelix and LCR did not (Fig. 6f). In EHD1/2/4 triple knockdown cells, ΔLCR still formed ER–PM contacts similar to control cells, indicating that the MORN domains can bind the PM independent of EHDs (Extended Data Fig. 6b). Pearson correlation coefficients revealed a significantly stronger correlation between EHD4 and 8MORN_LCR or 8MORN_LCR-αHelix compared with 8MORN-αHelix or LCR, suggesting that both 8MORN and LCR are necessary for JPH3's EHD4 interaction. It is worth noting that 8MORN-αHelix displays stronger colocalization with EHD4 than LCR (Fig. 6g), despite having weaker PM affinity, highlighting the role of MORN motifs in EHD interaction. As a control, mCherry-8MORN_LCR did not colocalize with clathrin-marked puncta on the PM (Fig. 6h and Extended Data Fig. 6c).

To further determine whether EHD4 interacts with 8MORN_LCR, we conducted co-immunoprecipitation studies. GFP-EHD4 was coexpressed with either mCherry-8MORN_LCR, mCherry-LCR or mCherry in HEK293T cells. Pulling down GFP-EHD4 with anti-GFP beads showed co-precipitation with mCherry-8MORN_LCR, but not with mCherry-LCR or mCherry (Fig. 6i). Overall, these results support a molecular model in which the curvature preference of JPH-mediated ER–PM contact is due to interactions between the N-terminal segment of JPH3 and EHDs.

Discussion

ER–PM contacts were discovered in the 1950s in striated muscle cells that have extensive T-tubule systems[60]. These contacts are prominent in striated muscle cells, occupying up to 50% of the T-tubule membranes[17] compared with 4–8% of the peripheral PM and even less in non-muscle cells. Surprisingly, little is known about the mechanism of such enrichment on T-tubule membranes. Our results suggest that T-tubule PM curvature spatially enriches ER–PM contacts. Using vertical nanobars, we showed that ER–PM contacts preferentially form at the nanobar ends rather than sidewalls, conclusively demonstrating that T-tubules enrich ER–PM contacts by the nature of their PM curvature, not by simply bringing the PM closer to the ER.

Our observation that PM curvature enriches JPH-mediated ER–PM contacts provides a perspective on the role of membrane curvature in ER–PM contact formation. Recent studies suggest that ER membrane curvature might play a role in lipid transfer at ER–PM contacts in yeast[61,62]. The asymmetric packing of lipid molecules in the outer leaflet of curved membranes is thought to accelerate lipid exchange[63]. Our finding that PM curvature promotes local ER–PM contact formation through curvature-sensing proteins may inspire discoveries about their effect on lipid transfer functions, beyond calcium signalling.

Our studies show that the MORN_LCR motifs interact with curvature-sensing EHDs on the PM, mediating JPH targeting of PM curvatures. Disrupting EHD localization by cholesterol extraction disturbed JPH3's curvature preference but not its PM targeting. This suggests two populations of JPH3-mediated ER–PM contacts: one dependent on EHDs and cholesterol and one independent of them. This aligns with the previous observation that JPHs cofractionate with both the caveolin-rich lipid rafts and the non-lipid raft domains[64].

In our studies, PM curvatures were generated by vertical nanostructures, whereas in vivo they are generated and stabilized by curvature-sculpturing and -sensing proteins such as bridging integrator 1 (BIN1), which are essential for T-tubule generation and stabilization[65,66]. We found that BIN1 knockdown by shRNAs (Extended Data Fig. 5c) decreased JPH3's curvature preference, albeit less significantly than EHD knockdowns (Extended Data Fig. 7). The potential coordination and synergy between EHDs and BIN1 in this process warrants further investigation.

Previous research showed that EHD proteins generate membrane tubules with diameters of 20–100 nm (refs. 47,48). In contrast, T-tubules in cardiomyocytes are larger, with a mean diameter of ~250 nm in rodents and ~400 nm in larger mammals[67], and our study shows a clear curvature preference of EHD for nanopillar- or nanobar-induced PM curvatures with diameters of 200–300 nm (Extended Data Figs. 5a and 6a). It is worth noting that although curvature sensing and curvature generation are often properties of the same proteins[68], they may involve different molecular interactions, with curvature sensing dominated by protein–membrane interactions and curvature generation involving protein oligomerization and scaffolding in addition to protein–membrane interactions[69–71]. Therefore, it is plausible that the same proteins may generate and sense membrane curvatures at different dimentional ranges. For instance, another curvature-sensing protein, FBP17, induces tubules of ~70 nm but sense curvatures up to 450 nm (refs. 72,73). Nevertheless, our study is based on observations of nanostructures 200–300 nm in diameter and the curvature preferences of ER–PM contact proteins such as JPHs and E-Syt2s beyond this range remain to be explored.

Fig. 6 | EHD proteins interact with JPHs and convey the PM curvature preference. a, Schematic of PM-targeting and curvature-sensing candidates in the JPH2 interactome. **b**, Representative images of GFP-JPH3 on nanobars with shRNA knockdown (KD) of scramble, clathrin, CAVIN1, CAV1/2 or EHD1/2/4. Left to right: BF images, protein fluorescence indicating shRNA transfection, GFP-JPH3, enlarged views of the regions shown in the yellow boxes and averaged nanobar images from multiple cells. Average cell numbers: scramble = 28, shCalthrin = 23, shCAVIN1 = 30, shCAV1/2 = 53 and shEHD1/2/4 = 55. Scale bars, 10 μm (whole cell), 5 μm (enlarged region) and 2.5 μm (average). **c**, GFP-JPH3 end-to-side ratios upon knockdown. The cell numbers were the same as in **b**. ****$P < 0.0001$; NS, $P > 0.9999$ (shClathrin), $P > 0.9999$ (shCAV1shCAV2) and $P = 0.0592$ (shCAVIN1). **d**,**e**, Distributions (**d**) and end-to-side ratios (**e**) of GFP-JPH3 in U2OS cells on nanobars before and after 10 mM methyl-β-cyclodextrin (MβCD) treatment at 37 °C for 30 min. Right: Averaged images of all bars in a single cell. Scale bars, 5 μm (cells) and 1 μm (averages); $n = 15$ cells per group. ****$P < 0.0001$. **f**, Representative images of U2OS cells coexpressing GFP/mCherry-EHD4 with the indicated JPH3 variants. The enlarged views are of the regions shown in the yellow boxes in the whole cell images to the left. Scale bars, 10 μm (whole cells) and 5 μm (enlarged regions). **g**, Pearson's correlation coefficients (PCCs) between coexpressed GFP/mCherry-EHD4 and the JPH3 variants shown in **f**. Cell numbers were: mCherry-8MORN_LCR = 21, GFP-8MORN_LCR-αHelix = 17, mCherry-LCR = 19 and GFP-8MORN-αHelix = 19. ****$P < 0.0001$; **$P = 0.0024$ (8MORN_LCR-αHelix versus 8MORN-αHelix); **$P = 0.0075$ (8MORN_LCR versus 8MORN-αHelix); *$P = 0.0174$ (8MORN-αHelix versus LCR); NS, $P = 0.9995$ (8MORN_LCR-αHelix versus 8MORN_LCR). **h**, PCCs for colocalization between mCherry-8MORN_LCR and GFP-EHD4 or between mCherry-8MORN_LCR and anti-clathrin; $n = 21$ cells per group. ****$P < 0.0001$. **i**, Co-immunoprecipitation (IP) from HEK cells expressing GFP-EHD4 and mCherry-8MORN_LCR or mCherry-LCR. GFP was pulled via GFP antibody beads and the immunoprecipitates were blotted with mCherry antibody. All the experiments were replicated independently three times with similar results. The data in **c**, **e**, **g** and **h** are presented as means ± s.d. Statistical significance was determined by Kruskal–Wallis test corrected with Dunn's multiple comparisons test (**c**), unpaired two-tailed Welch's *t*-test (**e** and **h**) or one-way Brown–Forsythe and Welch ANOVA test (**g**). Source numerical data and unprocessed blots are available Source data.

https://doi.org/10.1038/s41556-024-01511-x

JPHs and E-Syts are both ER–PM tethering proteins, but they show distinct preferences for PM curvatures. This may contribute to a previous observation in *Caenorhabditis elegans* where JPHs and E-Syts exhibit different localizations in presynaptic sites and display antagonistic effects on synaptic transmission[74]. Moreover, although E-Syts are ubiquitously expressed, JPHs are specific to excitable cells (muscle cells, neurons, T cells[75] and pancreatic β cells[76]) in which calcium dynamics is critical. JPH1 and JPH2 are expressed in muscle cells, whereas JPH3 and JPH4 are present in neurons and important for neuronal afterhyperpolarization currents[77,78]. In our studies, several JPH2 alterations

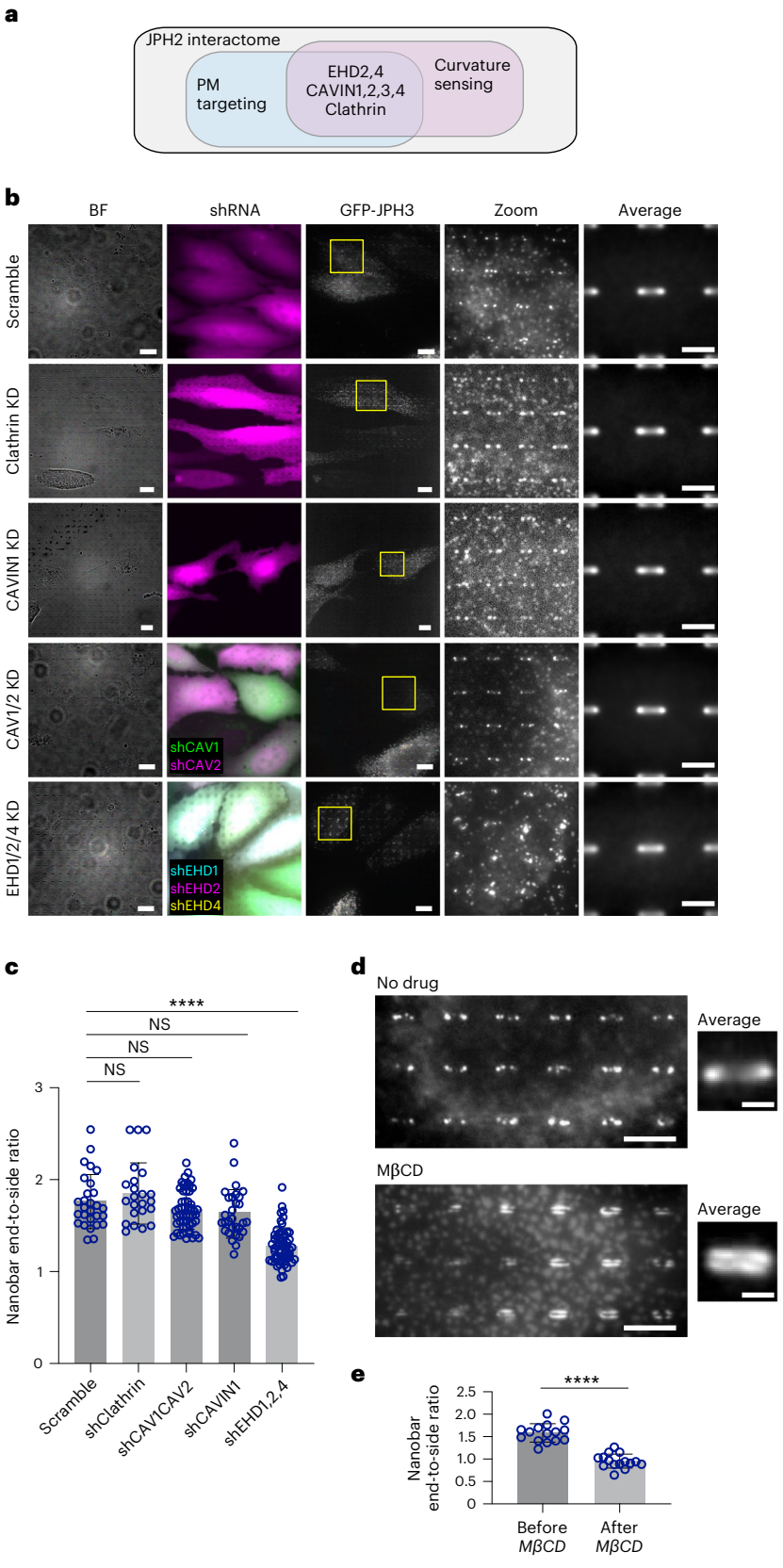

associated with hypertrophic cardiomyopathy impaired JPH2's targeting to membrane curvatures, which probably contributed to defects in calcium. Aside from those we examined, dozens of JPH2 alterations have been clinically associated with hypertrophic cardiomyopathy, dilated cardiomyopathy, arrhythmias and sudden cardiac death[7,79,80]. Furthermore, toxic aberrant transcription and loss of expression of JPH3 are linked to Huntington's disease-like 2 pathophysiology[81]. Our findings on the molecular mechanisms of JPHs will shed light on related mechanistic and therapeutic studies.

PM curvatures have been shown to affect various processes such as clathrin-mediated endocytosis, integrin adhesion, glycoprotein distribution, ion channel distribution and actin dynamics. Our finding that PM curvature directly regulates ER–PM contacts and thus cellular calcium responses opens a frontier in this exciting area.

Online content

Any methods, additional references, Nature Portfolio reporting summaries, source data, extended data, supplementary information, acknowledgements, peer review information; details of author contributions and competing interests; and statements of data and code availability are available at https://doi.org/10.1038/s41556-024-01511-x.

References

1. Wong, L. H., Gatta, A. T. & Levine, T. P. Lipid transfer proteins: the lipid commute via shuttles, bridges and tubes. *Nat. Rev. Mol. Cell Biol.* **20**, 85–101 (2019).
2. Scorrano, L. et al. Coming together to define membrane contact sites. *Nat. Commun.* **10**, 1287 (2019).
3. Gallo, A., Vannier, C. & Galli, T. Endoplasmic reticulum–plasma membrane associations: structures and functions. *Annu. Rev. Cell Dev. Biol.* **32**, 279–301 (2016).
4. Saheki, Y. & De Camilli, P. Endoplasmic reticulum–plasma membrane contact sites. *Annu. Rev. Biochem.* **86**, 659–684 (2017).
5. Stefan, C. J. Endoplasmic reticulum–plasma membrane contacts: principals of phosphoinositide and calcium signaling. *Curr. Opin. Cell Biol.* **63**, 125–134 (2020).
6. Piggott, C. A. & Jin, Y. Junctophilins: key membrane tethers in muscles and neurons. *Front. Mol. Neurosci.* **14**, 709390 (2021).
7. Parker, L. E., Kramer, R. J., Kaplan, S. & Landstrom, A. P. One gene, two modes of inheritance, four diseases: a systematic review of the cardiac manifestation of pathogenic variants in JPH2-encoded junctophilin-2. *Trends Cardiovasc. Med.* **33**, 1–10 (2023).
8. Khachaturian, Z. Calcium hypothesis of Alzheimer's disease and brain aging: a framework for integrating new evidence into a comprehensive theory of pathogenesis. *Alzheimers Dement.* **13**, 178–182.e17 (2017).
9. Popugaeva, E., Pchitskaya, E. & Bezprozvanny, I. Dysregulation of intracellular calcium signaling in Alzheimer's disease. *Antioxid. Redox Signal.* **29**, 1176–1188 (2018).
10. Huang, D.-X. et al. Calcium signaling regulated by cellular membrane systems and calcium homeostasis perturbed in Alzheimer's disease. *Front. Cell Dev. Biol.* **10**, 834962 (2022).
11. Lur, G. et al. Ribosome-free terminals of rough ER allow formation of STIM1 puncta and segregation of STIM1 from IP_3 receptors. *Curr. Biol.* **19**, 1648–1653 (2009).
12. Chung, G. H. C. et al. The ultrastructural organization of endoplasmic reticulum–plasma membrane contacts is conserved in epithelial cells. *Mol. Biol. Cell* **33**, ar113 (2022).
13. Lioudyno, M. I. et al. Orai1 and STIM1 move to the immunological synapse and are up-regulated during T cell activation. *Proc. Natl Acad. Sci. USA* **105**, 2011–2016 (2008).
14. Wu, Y. et al. Contacts between the endoplasmic reticulum and other membranes in neurons. *Proc. Natl Acad. Sci. USA* **114**, E4859–E4867 (2017).
15. Sun, J., Harion, R., Naito, T. & Saheki, Y. INPP5K and Atlastin-1 maintain the non-uniform distribution of ER–plasma membrane contacts in neurons. *Life Sci. Alliance* **4**, e202101092 (2021).
16. Lipp, P., Hüser, J., Pott, L. & Niggli, E. Spatially non-uniform Ca^{2+} signals induced by the reduction of transverse tubules in citrate-loaded guinea-pig ventricular myocytes in culture. *J. Physiol.* **497**, 589–597 (1996).
17. Bers, D. *Excitation—Contraction Coupling and Cardiac Contractile Force* (Springer Science & Business Media, 2001).
18. Dixon, R. E. Nanoscale organization, regulation, and dynamic reorganization of cardiac calcium channels. *Front. Physiol.* **12**, 810408 (2021).
19. Lyon, A. R. et al. Loss of T-tubules and other changes to surface topography in ventricular myocytes from failing human and rat heart. *Proc. Natl Acad. Sci. USA* **106**, 6854–6859 (2009).
20. McMahon, H. T. & Boucrot, E. Membrane curvature at a glance. *J. Cell Sci.* **128**, 1065–1070 (2015).
21. Yang, S. et al. Membrane curvature governs the distribution of Piezo1 in live cells. *Nat. Commun.* **13**, 7467 (2022).
22. Zhao, W. et al. Nanoscale manipulation of membrane curvature for probing endocytosis in live cells. *Nat. Nanotechnol.* **12**, 750–756 (2017).
23. Wang, X. et al. Membrane remodeling properties of the Parkinson's disease protein LRRK2. *Proc. Natl Acad. Sci. USA* **120**, e2309698120 (2023).
24. Zhang, W. et al. Curved adhesions mediate cell attachment to soft matrix fibres in three dimensions. *Nat. Cell Biol.* **25**, 1453–1464 (2023).
25. Hong, T. & Shaw, R. M. Cardiac T-tubule microanatomy and function. *Physiol. Rev.* **97**, 227–252 (2017).
26. Bers, D. M. Cardiac excitation–contraction coupling. *Nature* **415**, 198–205 (2002).
27. Paik, D. T. et al. Large-scale single-cell RNA-seq reveals molecular signatures of heterogeneous populations of human induced pluripotent stem cell-derived endothelial cells. *Circ. Res.* **123**, 443–450 (2018).
28. Rosenberg, P., Zhang, H., Bryson, V. G. & Wang, C. SOCE in the cardiomyocyte: the secret is in the chambers. *Pflugers Arch.* **473**, 417–434 (2021).
29. Chen, F., Tillberg, P. W. & Boyden, E. S. Optical imaging. Expansion microscopy. *Science* **347**, 543–548 (2015).
30. Nakamoto, M. L., Forró, C., Zhang, W., Tsai, C.-T. & Cui, B. Expansion microscopy for imaging the cell–material interface. *ACS Nano* **16**, 7559–7571 (2022).
31. Thul, P. J. et al. A subcellular map of the human proteome. *Science* **356**, eaal3321 (2017).
32. Giordano, F. et al. $PI(4,5)P_2$-dependent and Ca^{2+}-regulated ER–PM interactions mediated by the extended synaptotagmins. *Cell* **153**, 1494–1509 (2013).
33. Ding, Y. et al. Ratiometric biosensors based on dimerization-dependent fluorescent protein exchange. *Nat. Methods* **12**, 195–198 (2015).
34. Chang, C.-L. et al. Feedback regulation of receptor-induced Ca^{2+} signaling mediated by E-Syt1 and Nir2 at endoplasmic reticulum–plasma membrane junctions. *Cell Rep.* **5**, 813–825 (2013).
35. Wu, M. M., Buchanan, J., Luik, R. M. & Lewis, R. S. Ca^{2+} store depletion causes STIM1 to accumulate in ER regions closely associated with the plasma membrane. *J. Cell Biol.* **174**, 803–813 (2006).
36. Liou, J., Fivaz, M., Inoue, T. & Meyer, T. Live-cell imaging reveals sequential oligomerization and local plasma membrane targeting of stromal interaction molecule 1 after Ca^{2+} store depletion. *Proc. Natl Acad. Sci. USA* **104**, 9301–9306 (2007).
37. Liou, J. et al. STIM is a Ca^{2+} sensor essential for Ca^{2+}-store-depletion-triggered Ca^{2+} influx. *Curr. Biol.* **15**, 1235–1241 (2005).

38. Zhang, S. L. et al. STIM1 is a Ca^{2+} sensor that activates CRAC channels and migrates from the Ca^{2+} store to the plasma membrane. *Nature* **437**, 902–905 (2005).
39. Xu, P. et al. Aggregation of STIM1 underneath the plasma membrane induces clustering of Orai1. *Biochem. Biophys. Res. Commun.* **350**, 969–976 (2006).
40. Luik, R. M., Wang, B., Prakriya, M., Wu, M. M. & Lewis, R. S. Oligomerization of STIM1 couples ER calcium depletion to CRAC channel activation. *Nature* **454**, 538–542 (2008).
41. Takeshima, H., Komazaki, S., Nishi, M., Iino, M. & Kangawa, K. Junctophilins: a novel family of junctional membrane complex proteins. *Mol. Cell* **6**, 11–22 (2000).
42. Bennett, H. J. et al. Human junctophilin-2 undergoes a structural rearrangement upon binding PtdIns(3,4,5)P_3 and the S101R mutation identified in hypertrophic cardiomyopathy obviates this response. *Biochem. J.* **456**, 205–217 (2013).
43. Sajko, S. et al. Structures of three MORN repeat proteins and a re-evaluation of the proposed lipid-binding properties of MORN repeats. *PLoS ONE* **15**, e0242677 (2020).
44. Yang, Z. F. et al. Structures of the junctophilin/voltage-gated calcium channel interface reveal hot spot for cardiomyopathy mutations. *Proc. Natl Acad. Sci. USA* **119**, e2120416119 (2022).
45. Landstrom, A. P. et al. Mutations in *JPH2*-encoded junctophilin-2 associated with hypertrophic cardiomyopathy in humans. *J. Mol. Cell. Cardiol.* **42**, 1026–1035 (2007).
46. Feng, W. et al. Identifying the cardiac dyad proteome in vivo by a BioID2 knock-in strategy. *Circulation* **141**, 940–942 (2020).
47. Daumke, O. et al. Architectural and mechanistic insights into an EHD ATPase involved in membrane remodelling. *Nature* **449**, 923–927 (2007).
48. Melo, A. A. et al. Cryo-electron tomography reveals structural insights into the membrane remodeling mode of dynamin-like EHD filaments. *Nat. Commun.* **13**, 7641 (2022).
49. Kovtun, O. et al. Structural insights into the organization of the cavin membrane coat complex. *Dev. Cell* **31**, 405–419 (2014).
50. Tillu, V. A. et al. Cavin1 intrinsically disordered domains are essential for fuzzy electrostatic interactions and caveola formation. *Nat. Commun.* **12**, 931 (2021).
51. Matthaeus, C. et al. The molecular organization of differentially curved caveolae indicates bendable structural units at the plasma membrane. *Nat. Commun.* **13**, 7234 (2022).
52. Posey, A. D. Jr et al. EHD1 mediates vesicle trafficking required for normal muscle growth and transverse tubule development. *Dev. Biol.* **387**, 179–190 (2014).
53. Hall, T. E. et al. In vivo cell biological screening identifies an endocytic capture mechanism for T-tubule formation. *Nat. Commun.* **11**, 3711 (2020).
54. Lo, H. P. et al. The caveolin–cavin system plays a conserved and critical role in mechanoprotection of skeletal muscle. *J. Cell Biol.* **210**, 833–849 (2015).
55. Lo, H. P. et al. Cavin4 interacts with Bin1 to promote T-tubule formation and stability in developing skeletal muscle. *J. Cell Biol.* **220**, e201905065 (2021).
56. Minamisawa, S. et al. Junctophilin type 2 is associated with caveolin-3 and is down-regulated in the hypertrophic and dilated cardiomyopathies. *Biochem. Biophys. Res. Commun.* **325**, 852–856 (2004).
57. Golini, L. et al. Junctophilin 1 and 2 proteins interact with the L-type Ca^{2+} channel dihydropyridine receptors (DHPRs) in skeletal muscle. *J. Biol. Chem.* **286**, 43717–43725 (2011).
58. Saeki, T., Suzuki, Y., Yamamura, H., Takeshima, H. & Imaizumi, Y. A junctophilin–caveolin interaction enables efficient coupling between ryanodine receptors and BK_{Ca} channels in the Ca^{2+} microdomain of vascular smooth muscle. *J. Biol. Chem.* **294**, 13093–13105 (2019).
59. Morén, B. et al. EHD2 regulates caveolar dynamics via ATP-driven targeting and oligomerization. *Mol. Biol. Cell* **23**, 1316–1329 (2012).
60. Porter, K. R. & Palade, G. E. Studies on the endoplasmic reticulum. III. Its form and distribution in striated muscle cells. *J. Biophys. Biochem. Cytol.* **3**, 269–300 (1957).
61. Collado, J. et al. Tricalbin-mediated contact sites control ER curvature to maintain plasma membrane integrity. *Dev. Cell* **51**, 476–487.e7 (2019).
62. Hoffmann, P. C. et al. Tricalbins contribute to cellular lipid flux and form curved ER–PM contacts that are bridged by rod-shaped structures. *Dev. Cell* **51**, 488–502.e8 (2019).
63. Machida, K. & Ohnishi, S. I. Effect of bilayer membrane curvature on activity of phosphatidylcholine exchange protein. *Biochim. Biophys. Acta* **596**, 201–209 (1980).
64. Wei, E. Q. et al. Inducible *Fgf13* ablation enhances caveolae-mediated cardioprotection during cardiac pressure overload. *Proc. Natl Acad. Sci. USA* **114**, E4010–E4019 (2017).
65. Lee, E. et al. Amphiphysin 2 (Bin1) and T-tubule biogenesis in muscle. *Science* **297**, 1193–1196 (2002).
66. Tjondrokoesoemo, A. et al. Disrupted membrane structure and intracellular Ca^{2+} signaling in adult skeletal muscle with acute knockdown of Bin1. *PLoS ONE* **6**, e25740 (2011).
67. Rog-Zielinska, E. A. et al. Species differences in the morphology of transverse tubule openings in cardiomyocytes. *Europace* **20**, iii120–iii124 (2018).
68. Baumgart, T., Capraro, B. R., Zhu, C. & Das, S. L. Thermodynamics and mechanics of membrane curvature generation and sensing by proteins and lipids. *Annu. Rev. Phys. Chem.* **62**, 483–506 (2011).
69. Sorre, B. et al. Nature of curvature coupling of amphiphysin with membranes depends on its bound density. *Proc. Natl Acad. Sci. USA* **109**, 173–178 (2012).
70. Simunovic, M. & Voth, G. A. Membrane tension controls the assembly of curvature-generating proteins. *Nat. Commun.* **6**, 7219 (2015).
71. Simunovic, M., Voth, G. A., Callan-Jones, A. & Bassereau, P. When physics takes over: BAR proteins and membrane curvature. *Trends Cell Biol.* **25**, 780–792 (2015).
72. Lou, H.-Y. et al. Membrane curvature underlies actin reorganization in response to nanoscale surface topography. *Proc. Natl Acad. Sci. USA* **116**, 23143–23151 (2019).
73. Su, M. et al. Comparative study of curvature sensing mediated by F-BAR and an intrinsically disordered region of FBP17. *iScience* **23**, 101712 (2020).
74. Piggott, C. A. et al. *Caenorhabditis elegans* junctophilin has tissue-specific functions and regulates neurotransmission with extended-synaptotagmin. *Genetics* **218**, iyab063 (2021).
75. Woo, J. S. et al. Junctophilin-4, a component of the endoplasmic reticulum–plasma membrane junctions, regulates Ca^{2+} dynamics in T cells. *Proc. Natl Acad. Sci. USA* **113**, 2762–2767 (2016).
76. Li, L. et al. Junctophilin-3 expresses in pancreatic beta cells and is required for glucose-stimulated insulin secretion. *Cell Death Dis.* **7**, e2275 (2016).
77. Sahu, G. et al. Junctophilin proteins tether a Cav1–RyR2–KCa3.1 tripartite complex to regulate neuronal excitability. *Cell Rep.* **28**, 2427–2442.e6 (2019).
78. Moriguchi, S. et al. Functional uncoupling between Ca^{2+} release and afterhyperpolarization in mutant hippocampal neurons lacking junctophilins. *Proc. Natl Acad. Sci. USA* **103**, 10811–10816 (2006).
79. Lehnart, S. E. & Wehrens, X. H. T. The role of junctophilin proteins in cellular function. *Physiol. Rev.* **102**, 1211–1261 (2022).
80. Hall, D. D., Takeshima, H. & Song, L.-S. Structure, function, and regulation of the Junctophilin family. *Annu. Rev. Physiol.* **86**, 123–147 (2024).

81. Krause, A. et al. Junctophilin-3 (JPH3) expansion mutations causing Huntington disease like 2 (HDL2) are common in South African patients with African ancestry and a Huntington disease phenotype. *Am. J. Med. Genet. B* **168**, 573–585 (2015).

[1]Department of Chemistry, Stanford University, Stanford, CA, USA. [2]Wu Tsai Neurosciences Institute and ChEM-H Institute, Stanford University, Stanford, CA, USA. [3]Stanford Cardiovascular Institute, Stanford University, Stanford, CA, USA. [4]Department of Physiology, University of Texas Southwestern Medical Center, Dallas, TX, USA. [5]Tissue Electronics, Istituto Italiano di Tecnologia, Naples, Italy. [6]Faculty of Electrical Engineering and Information Technology, RWTH Aachen University, Aachen, Germany. [7]Institute of Biological Information Processing—Bioelectronics (IBI-3), Forschungszentrum, Jülich, Germany. [8]Department of Medicine, Division of Cardiology, Stanford University, Stanford, CA, USA. [9]Department of Radiology, Stanford University, Stanford, CA, USA. [10]Present address: Departments of Physiology and Medicine, Medical College of Wisconsin, Milwaukee, WI, USA. [11]Present address: Department of Biomedical Engineering, University of North Texas, Denton, TX, USA. [12]Present address: Department of Chemical and Nano Engineering, University of California, San Diego, San Diego, CA, USA. ✉e-mail: bcui@stanford.edu

Methods

Ethics

iPSCs were obtained from Stanford Cardiovascular Institute Biobank and used per Institutional Review Board/Stem Cell Research Oversight Panel guidelines, adhering to federal, state and Stanford University human stem cell research policies. The use of laboratory rats was approved by the Stanford University Administrative Panel on Laboratory Animal Care and adhered to relevant ethical regulations.

Nanopillar and nanobar fabrication

Fused quartz substrates were cleaned using acetone and isopropanol, sonicated to eliminate contaminants and dried at 180 °C. Subsequently, a 275 nm layer of 9% CSAR 62 electron beam resist was spin-coated onto the substrate and baked at 180 °C for 3 min, then a 100 nm conductive Electra 92 layer was applied and baked for an additional 3 min. Using the Raith Voyager lithography system, nanopatterned pillars and bars were fabricated while compensating for proximity effects. After lithography exposure, the Electra 92 conductive layer was removed in deionized water and xylene development revealed the nanopatterns. A 120 nm chromium (Cr) masking layer was evaporated onto the substrate, followed by plasma etching using the Plasma Therm Versaline LL ICP Dielectric Etcher to reach a depth of 1,500 nm. Lastly, the Cr layer was removed with a Cr etchant. The substrate dimensions were characterized using a Magellan scanning electron microscope.

Cell culture

U2OS cells (HTB-96; American Type Culture Collection (ATCC)), HeLa cells (CCL-2; ATCC) and HEK293T cells (CRL-3216; ATCC) were cultured in DMEM (11965-092; Gibco) supplemented with 10% (vol/vol) foetal bovine serum (FBS) (F4135; Sigma–Aldrich). iCells (01434; FUJIFILM Cellular Dynamics), rat embryonic CMs and iPSC-CMs were maintained in RPMI (11875-093; Gibco) with B27 supplement (50:1; 17504-044; Gibco). HL-1 cells were obtained from the laboratory of W. C. Claycomb at Louisiana State University and maintained in Claycomb medium supplemented with 10% FBS.

iPSC-CM differentiation

Human iPSCs were obtained from Stanford Cardiovascular Institute and cultured in E8 medium (Gibco, Life Technologies) on six-well plates coated with Matrigel (Corning). Cells were passaged at a 1:12 ratio after 5 min of incubation with Accutase (Sigma–Aldrich) at 37 °C. After replating, the E8 medium was supplemented with 10 μM Y-27632 ROCK inhibitor (Selleck Chemicals) for 24 h. Subsequently, the medium was changed to standard E8 medium with daily medium changes. For differentiation into CMs, hiPSCs were seeded at a 1:12 ratio and cultured until they reached 85% confluence. Differentiation was initiated by changing the medium to RPMI supplemented with B27 without insulin (Life Technologies) and 6 μM CHIR-99021 (Selleck Chemicals). At 48 h post-induction, the medium was switched to RPMI-B27 without insulin for 24 h and then supplemented with 5 μM IWR-1 (Selleck Chemicals) for another 48 h. Metabolic purification of CMs was conducted on day 11 using RPMI-B27 without D-glucose (Life Technologies) for 96 h. After purification, CMs were maintained in RPMI-B27 for future experiments.

Cell culture on nanochips

Before seeding cells, nanochips (nanopillar and nanobar) were treated with air plasma (Harrick Plasma) at high power for 10 min, then the nanochips were coated with 0.1 mg ml^{-1} poly-L-lysine in phosphate-buffered saline (PBS) at room temperature for 30 min, followed by 3× PBS washes, incubation with 0.5% (vol/vol) glutaraldehyde (G6257; Sigma–Aldrich) in PBS at room temperature for 10–15 min, another three PBS washes and incubation with the desired extracellular matrix protein. Specifically for U2OS, HeLa and HEK293T cells, the chips were incubated with 0.1% (mass/vol) gelatin combined with 20 μg ml^{-1} human plasma fibronectin (341635; Sigma–Aldrich) in PBS at 37 °C for 1 h followed by three PBS washes. If fluorescence imaging was needed, the chips were then treated with 5 mg ml^{-1} sodium borohydride in PBS at room temperature for 5 min to quench the autofluorescence from glutaraldehyde followed by three PBS washes before seeding the cells. For iPSC-CMs, rat embryonic CMs and iCells, the extracellular matrix protein used was Matrigel (356231; Corning) diluted with ice-cold DMEM/F-12 + GlutaMAX (10565-018; Gibco) at a 1:200 ratio, with incubation at 37 °C for 1 h overnight. After removing the extra Matrigel, cells were seeded on the chips with RPMI + B27 + 10% KnockOut Serum Replacement Multi-Species (A31815-01; Gibco) and changed to maintenance medium after 24 h.

Rat embryonic CM isolation

Freshly dissected hearts from E18 Sprague Dawley rats (Charles River Laboratories) with no bias on sex were cut into four pieces and washed with HHBSS buffer (HBSS (14025126; Gibco) + 10 mM HEPES + 1 mM glucose). Cardiomyocytes were isolated in TrypLE Select 10× (A12177-01; Gibco) for 30 min at 37 °C with agitation. Isolated cardiomyocytes were cultured in 10% KnockOut Serum Replacement in RPMI supplemented with B27 overnight, which was changed to RPMI + B27 maintenance medium afterwards.

Antibodies and reagents

Anti-junctophilin-2 antibody (HPA052646; Sigma–Aldrich), anti-RyR2 antibody (NB1202827; Novus Bio), anti-Cav1.2 antibody (C1103; Sigma–Aldrich), anti-α-actinin antibody (A7811; Sigma–Aldrich), anti-calreticulin antibody (PA3-900; Invitrogen) and anti-EHD4 antibody (50-172-7111; Thermo Fisher Scientific) were used at dilutions of 1:300, 1:400, 1:300, 1:1,000, 1:400 and 1:400, respectively, for immunofluorescence. Anti-EHD2 antibody (CSB-PA873710LA01HU-20UG; Cusabio) was used at a dilution of 1:300 for immunofluorescence and 1:1,000 for immunoblotting. Anti-caveolin-1 antibody (sc-70516; Santa Cruz Biotechnology), anti-caveolin-2 antibody (CSB-PA004572LA01HU-20UG; Cusabio), anti-EHD1 antibody (CSB-PA884470LA01HU-20UG; Cusabio), anti-clathrin antibody (MA1-065; Invitrogen) and anti-BIN1 antibody (SAB1408547; Sigma–Aldrich) were all used at 1:1,000 for immunoblotting. Alexa Fluor 594-goat anti-rabbit IgG (A11012; Invitrogen) and Alexa Fluor 647-goat anti-mouse IgG (A32728; Invitrogen) were used as secondary antibodies at a dilution of 1:1,000. Anti-GFP antibody (A-11122; Invitrogen), anti-mCherry antibody (SAB2702291; Sigma–Aldrich), horseradish peroxidase (HRP)-linked goat anti-rabbit IgG (H + L) antibody (7074; Cell Signaling Technology) and HRP-linked goat anti-mouse IgG (H + L) antibody (7076; Cell Signaling Technology) were used at a dilution of 1:1,000 for immunoblotting. Methyl-β-cyclodextrin (C4555) and Tg (T9033; Sigma–Aldrich) were diluted as indicated in the main text.

Plasmids

Details of the plasmids used can be found in Supplementary Table 2. The plasmids we made in this research are all readily available upon request to the corresponding author.

Cell transfection

For the imaging experiments, U2OS and HEK293T cells were transfected through electroporation (Lonza Amaxa Biosystems Nucleofector II) using pre-installed protocols. For each transfection, ~0.5 million cells were electroporated with 0.2–0.5 μg plasmid DNA in 100 μl Electroporation buffer II (88 mM KH_2PO_4 and 14 mM $NaHCO_3$ (pH 7.4)) freshly supplemented with 2 μl Electroporation buffer I (360 mM ATP + 600 mM $MgCl_2$). HeLa cells were transfected with Lipofectamine 2000 (11668-019; Invitrogen). Plasmid DNA (0.5–1.0 μg) was used for each transfection of 0.2 million cells according to the reagent protocol.

Lentiviral particle packaging

Lentivirus was generated in HEK293T cells at ~70–80% confluency in six-well plates. The medium was switched to pre-warmed DMEM

before transfection. Each well received 0.8 µg psPAX2 plasmids, 0.7 µg pMD2.G plasmids and 1.5 µg transfer plasmid with specific complementary DNA or shRNA with Lipofectamine 2000. The media was switched to DMEM + 10% FBS + 1 mM Sodium Pyruvate (11360; Gibco) after 4–6 h. Virus-containing medium was collected after 24 h, filtered through 0.45 µm polyvinylidene difluoride filters (Millipore) and added to targeted cells. Lentiviral particles were used for all of the transfections in iPSC-CMs and knockdowns in U2OS cells.

shRNA interference experiments

shRNA sequences were cloned into a third-generation transfer plasmid pLKO.1-TRC cloning vector following Addgene's protocol. The sequences of shRNA oligos were either from Sigma–Aldrich's predesigned shRNA or from Addgene (Supplementary Table 2). The puromycin-resistant sequence in the pLKO.1 vector was replaced with a sequence encoding BFP/mCherry/iRFP to fluorescently label cells that were transfected or transduced. The knockdown effects were examined on day 3 after lentiviral transfection.

Western blotting

Four days after shRNA lentiviral infection, U2OS cells were lysed in RIPA buffer (25 mM Tris-HCl, 150 mM NaCl, 1% Triton X-100, 1% sodium deoxycholate and 0.1% sodium dodecyl sulfate) with protease and phosphatase inhibitor cocktails (04693159001 and 04906837001; Roche) for 30 min on ice with vortexing every 5–10 min. The lysate was then centrifuged at 12,000*g* and 4 °C for 10 min. The supernatants were then boiled at 95 °C for 10 min, subjected to sodium dodecyl sulfate–polyacrylamide gel electrophoresis and transferred to nitrocellulose membranes using the Trans-Blot Turbo Transfer System (1704150; Bio-Rad). Membranes were stained with Ponceau solution (5% vol/vol glacial acetic acid and 0.1% wt/vol Ponceau S) to confirm the equal loading then blocked with 5% milk in TBS-T buffer (20 mM Tris, 150 mM NaCl, with 0.1% w/v Tween 20, pH 7.6) for 30 min and incubated with the indicated antibody diluted in 3% bovine serum albumin (BSA) in TBS-T overnight at 4 °C. Protein bands were visualized using HRP-conjugated secondary antibody and chemiluminescence with Azure Imaging Systems (Azure Biosystems).

Co-immunoprecipitation assay

HEK293T cells were co-transfected with mCherry-8MORN_LCR, mCherry-LCR or mCherry alone, together with GFP-EHD4, via electroporation and then cultured overnight. Confluent cells were trypsinized, harvested by spinning, washed with ice-cold PBS and mixed with freshly prepared 0.5 mM 3,3′-dithiobis(succinimidyl propionate) (Sigma–Aldrich) in 1× PBS for 40 min at room temperature. The reaction was quenched with ice-cold 25 mM Tris-HCl buffer for 20 min. After centrifugation, cell pellets were lysed in 1× RIPA buffer supplemented with protease (cOmplete; Roche) and phosphatase inhibitors (PhosSTOP; Roche) for 1 h at 4 °C. The lysates were then subjected to sonication at a pulse of 20–25% amplitude for 10 s followed by 25 s of incubation on ice. The sonication–incubation cycle was repeated twice. Subsequently, the lysates were mixed with equilibrated GFP-Trap magnetic agarose (ChromoTek) and incubated overnight at 4 °C. The bead–protein complexes were harvested by centrifugation and washed five times with PBS. To elute and denature proteins, the bead–protein pellets were resuspended in a 2× Laemmli sample buffer (with β-mercaptoethanol) and boiled for 5–10 min at 95 °C. The samples were analysed by sodium dodecyl sulfate–polyacrylamide gel electrophoresis and western blotting with anti-GFP and anti-mCherry antibodies.

Immunofluorescence

iPSC-CMs were seeded on nanochips, which had both nanopillar regions and flat regions on the same chip, ensuring imaging of both flat surfaces and nanopillar surfaces under the same conditions. Cells grew on nanochips for 3–4 d. For GFP-CAAX transfection, the iPSC-CMs on nanochips were cultured in seeding medium for 1 d, then switched to GFP-CAAX lentivirus medium for 1 d followed by maintenance medium for another 2 d. Samples were then fixed with 4% paraformaldehyde for 15 min, quenched with 5 mg ml^{-1} sodium borohydride in PBS for 5 min, permeabilized with 0.1% Triton X-100 for 10 min and blocked with 3% BSA for 30 min at room temperature. Three PBS washes were performed inbetween each step. Primary antibodies diluted in 3% BSA were then incubated overnight at 4 °C. The samples were then washed with PBS for 5 min three times and then stained with the secondary antibodies for 1 h at room temperature. Samples were subjected to fluorescence imaging or ExM processing afterwards.

FIB-SEM imaging

The procedure was adapted from a previous study by our group[82]. Nanochips with cells were first rinsed with 0.1 M sodium cacodylate buffer (Electron Microscopy Sciences) and fixed at 4 °C overnight using 3.2% glutaraldehyde (Sigma–Aldrich). Subsequently, specimens underwent post-fixation with 4% osmium tetroxide and 2% potassium ferrocyanide (Electron Microscopy Sciences) for 1 h, followed by 1% thiocarbohydrazide (Electron Microscopy Sciences) for 20 min and 2% aqueous osmium tetroxide for 30 min. After rinsing twice with distilled water, samples were incubated overnight with syringe-filtered 4% aqueous uranyl acetate (Electron Microscopy Sciences; en-bloc step). Dehydration was achieved through an increasing ethanol series (10–30–50–70–90–100%; each step lasting 5–10 min), followed by specimen infiltration with epoxy-based resin using various ethanol-to-resin ratios (1:3 for 3 h, 1:2 for 3 h, 1:1 overnight, 2:1 for 3 h and 3:1 for 3 h). Finally, samples were infiltrated with 100% resin overnight at room temperature and, after the removal of excess resin, polymerization was carried out at 60 °C overnight.

Prepared samples were metal sputtered and loaded in a dual-beam Helios NanoLab 600i FIB-SEM (FEI) vacuum chamber. Secondary SEM imaging used a voltage of 3–5 kV and a current of 21 pA–1.4 nA. Cross-section imaging employed a beam acceleration with a voltage of 2–10 kV and a current of 0.17–1.4 nA using a backscattered electron detector. Preservation of regions of interest involved double platinum layer deposition via in situ sputtering. Trenches were etched at an acceleration voltage of 30 kV and a current of 9.1–0.74 nA, followed by fine polishing of the resulting cross-sections using a voltage of 30 kV and a current of 80 pA.

ExM imaging

ExM was performed as previously described[30]. Cells were cultured on nanopillar chips, fixed and immunostained. The samples were then incubated overnight at room temperature in a 1:100 dilution of Acryloyl-X, SE (6-((acryloyl)amino)hexanoic acid, succinimidyl ester; A20770; Invitrogen) in PBS. The samples were then washed with PBS followed by a 15 min incubation at room temperature in gelation solution (19% (wt/wt) sodium acrylate, 10% (wt/wt) acrylamide and 0.1% (wt/wt) *N*,*N*′-methylenebisacrylamide). Gelation solution supplemented with 0.5% *N*,*N*,*N*′,*N*′-tetramethylenediamine and 0.5% ammonium persulfate (APS) was then prepared and briefly vortexed. The gelation solution, *N*,*N*,*N*′,*N*′-tetramethylenediamine and APS were kept on ice before combining, and APS was added last to initiate gelation. Nanochips were then flipped cell side down onto a 70 µl drop of this supplemented gelation solution on parafilm and incubated at 37 °C for 1 h. The nanochip with the hydrogel still attached was then incubated in a 1:100 dilution of proteinase K in digestion buffer (50 mM Tris-HCl (pH 8), 1 mM EDTA, 0.5% Triton X-100 and 1 M NaCl) for 7 h at 37 °C. The hydrogel at this point had expanded and detached from the nanochip. The hydrogel was then soaked twice in Milli-Q water for 30 min and then left to incubate overnight in Milli-Q water at 4 °C. Before imaging, excess water on the hydrogels was carefully removed using a Kimwipe. The hydrogels were then mounted onto poly-L-lysine-coated glass coverslips cell side down to prevent sliding during imaging.

ExM analysis

The expanded sample was imaged with a 40× water lens on a confocal microscope. *Z*-stack images were taken every 0.3 µm with a 1.2 Airy Unit. The pixel size in the final image was 0.0777 in *x* and *y* and 0.3 µm in *z*. The *z* direction was scaled up ~3.86 times (0.3/0.0777) for display (Fig. 2d,f,g) to match *x* and *z* dimension visually. The *x*–*z* view displayed in Fig. 2f is an average projection of the *x*–*z* view of five neighbouring pixels in *y*.

For pillar-to-flat ratio quantification (Fig. 2h), the background was subtracted for both CAAX and JPH2 channels and single pillars were identified using the in-house MATLAB code. Pillar and flat region intensities were quantified from average projected *x*–*z* images. Specifically, the pillar intensity was calculated as the average of the 25 consecutive *y* slices centred on each pillar's central and the flat intensity was the average of 40 consecutive *y* slices near each pillar. Five or six such regions in each row were averaged as one data point. Ratios of pillar-to-flat intensities were normalized by the average ratio of the CAAX to set the CAAX pillar-to-flat ratio to one.

To quantify the JPH2 density increase from flat to pillar surfaces, we calculated the ratio of JPH2/CAAX at the pillar to that of JPH2/CAAX at the flat surfaces for each data point.

Fluorescence imaging

Transfected U2OS, HeLa and HEK293T cells were imaged live in Ringer's buffer (155 mM NaCl, 4.5 mM KCl, 2 mM $CaCl_2$, 1 mM $MgCl_2$, 5 mM HEPES and 10 mM D-glucose (pH 7.4)) or fixed in PBS at room temperature unless otherwise stated. Nanochips were placed on 35 mm glass-bottom dishes (D35-20-1-N; Cellvis) with the cell side down for 100× (1.40 NA) magnification single-image capturing and on 0.15 mm thin nanochips for 60× magnification time-lapse imaging. Confocal and expansion microscopy images were taken under a Nikon A1R confocal microscope controlled by Nikon NIS-Elements AR software, equipped with 405, 488, 561 and 633 nm lasers for excitation under a 40× water objective (WD = 0.61 mm; 1.15 NA). *Z*-stack images were taken every 0.3 µm with a 1.2 Airy unit. All other fluorescence images were taken under an epi-fluorescence microscope (Leica THUNDER Ready DMi8 system) equipped with a Leica LED8 system and a K8 Scientific CMOS microscope camera and controlled by Leica LAS X software.

Pearson's correlation coefficient analysis

Cells were co-transfected with GFP- or mCherry-labelled proteins. ImageJ software was used for Pearson's correlation coefficient analysis. A 200 pixel rolling ball background subtraction was applied to both channels and cells was manually cropped along the cell boundary, excluding the nucleus. The Pearson's correlation coefficient between the two channels was then calculated.

ER calcium depletion assay

For the STIM1 and ORAI1 translocation experiments, cells were transfected with the indicated probes and seeded on thin nanochips 1 d before imaging. Cells were first imaged in Ringer's solution, then a final concentration of 2 µM Tg was added and images were taken at 1 frame per second for 10 min. For kinetic analysis, we selected the ORAI1 dots that were newly assembled after Tg treatment and remained stationary, indicative of a contact localization, instead of intracellular vesicles.

Nanopillar and nanobar averaging and end-to-side ratio quantification

Nanopillars and nanobars were automatically identified and averaged within each cell using custom MATLAB code, as previously described[83]. Multiple cell average images (Figs. 1e,i,k, 3g, 4e, 5k, 6b and Extended Data Figs. 4b, 5g,h, 6a, and 7) were generated by normalization and averaging of the averaged nanopillar or nanobar images from different cells using ImageJ. The nanobar end-to-side ratio was determined by dividing the end intensity by the side intensity from the averaged nanobar image of each cell, with the background subtracted. For ER–PM tethering protein quantification, cells with expression levels either too low (less than 2× the background intensity) or too high (patch diameter > 1 µm) were excluded to avoid artefacts caused by the expression level. For all JPH3 constructs without a transmembrane domain (constructs in the right graph of Fig. 5l) and CAAX in Fig. 5l, a 50 pixel rolling ball was applied before quantification to subtract the cytosolic background.

Protein interactome data analysis

The protein interactome of JPH2 in cardiomyocytes, as identified by the proximity labelling method in a previous study by Feng et al.[46], was subjected to analysis using Metascape.org. The proteins were annotated for biological process (Gene Ontology), protein function (Protein Atlas) and subcellular location (Protein Atlas). Proteins associated with the PM or endosomes were grouped as PM-associated proteins. The analysis revealed that 38 proteins prominently localized to the PM, 30 proteins had additional PM localization (including two with endosome associations) and three associated with endosomes. Manual assessments identified seven of these proteins as having established roles in sensing or generating PM curvatures (Supplementary Table 1). The U2OS cell expression of these proteins was assessed by transcripts per million (TPM) values from RNA sequencing data in previous research[31]. Genes with TPM levels above 15 TPM were knocked down. EHD1, not identified in the list, was also knocked down, together with EHD2 and EHD4, to prevent complementary effects.

Statistics and reproducibility

Statistical analysis was conducted using Prism 9 software (GraphPad). No statistical methods were used to pre-determine sample sizes, but our sample sizes were similar to those reported in previous publications. Normality in each sample group was assessed with the D'Agostino–Pearson normality test ($\alpha = 0.05$). For datasets that passed the normality test (that is, parametric datasets), we employed an unpaired two-tailed Welch's *t*-test to evaluate the significance of the difference between two groups, and one-way Brown–Forsythe and Welch analysis of variance tests corrected with Dunnett's T3 multiple comparisons test to compare more than two groups. For datasets that did not pass the normality test (namely non-parametric datasets), we used a two-tailed Mann–Whitney test to compare two groups or a Kruskal–Wallis test corrected with Dunn's multiple comparisons test to compare more than two groups. Exact *P* values are provided in the figure captions along with 95% confidence intervals. All experiments were replicated independently at least twice with a minimum of three cells per replication. Specific sample sizes (*n* numbers) and repeat numbers are indicated in the figure captions. No data were excluded from the tests except for quantifications in Fig. 5, for which we excluded improper data, as detailed in the section 'Nanopillar and nanobar averaging and end-to-side ratio quantification'. The experiments were not randomized. The investigators were not blinded to allocation during the experiments and outcome assessment.

Reporting summary

Further information on research design is available in the Nature Portfolio Reporting Summary linked to this article.

Data availability

The referenced dataset of the JPH2 bio-interactome is from the Mass Spectrometry Interactive Virtual Environment (MSV000084352)[46] and the referenced protein atlas is from https://www.proteinatlas.org. Source data are provided with this paper. All of the other data supporting the findings of this study are available from the corresponding author upon reasonable request.

Code availability

The custom MATLAB code used in this study for nanopillar/nanobar imaging analysis was published in previous research by our laboratory[24] and is available from GitHub (https://github.com/wzhang5publication/Data-analysis). Additional information is available from the corresponding author upon reasonable request.

References

82. Santoro, F. et al. Revealing the cell–material interface with nanometer resolution by focused ion beam/scanning electron microscopy. *ACS Nano* **11**, 8320–8328 (2017).
83. Lu, C.-H. et al. Membrane curvature regulates the spatial distribution of bulky glycoproteins. *Nat. Commun.* **13**, 3093 (2022).

Acknowledgements

We thank R. Lewis and R. Qiu from Stanford University for insightful discussions and for sharing the STIM1 and ORAI1 plasmids; C. Bertozzi from Stanford University for sharing the confocal microscope; and G.-N. Tseng from Virginia Commonwealth University for sharing the JPH2 plasmids. This study was supported by National Institutes of Health grants R35GM141598, R01HL165491, 1R01NS121934, R01 HL150693, R01 HL145676, R01 HL113006 and R01 GM144479. This work was also supported by the Stanford Sarafan ChEM-H Chemistry/Biology Interface Program (1T32GM139791-01A1 to L.A.V.), a Stanford University Center for Molecular Analysis and Design fellowship (to C.-H.L.), a National Institutes of Health Biotechnology Training Grant fellowship (to M.L.N.) and American Heart Association's Second Century Early Faculty Independence Award (to C.L.). J.L. is a Sowell Family Scholar in Medical Research. The nanofabrication in this work was performed at the Stanford Nanofabrication Facility under the National Science Foundation National Nanotechnology Coordinated Infrastructure program and Stanford Nano Shared Facilities supported by the National Science Foundation under award ECCS-2026822.

Author contributions

Y.Y. and B.C. conceived of the study and designed the experiments. Y.Y. and L.A.V. performed the cell and imaging experiments. Y.Y., L.A.V., W.Z. and W.-R.L. constructed the plasmids. C.-H.L. performed the immunoprecipitation experiment. M.L.N. and L.A.V. performed the ExM experiment. C.-T.T. and Z.J. fabricated the nanostructures and performed the SEM characterization. C.L. and H.Y. performed the iPSC-CM differentiation experiments. F.S. conducted the FIB-SEM experiments. Y.Y., B.C., J.L. and J.C.W. discussed the results and wrote the paper with feedback from all authors.

Competing interests

The authors declare no competing interests.

Additional information

Extended data is available for this paper at https://doi.org/10.1038/s41556-024-01511-x.

Supplementary information The online version contains supplementary material available at https://doi.org/10.1038/s41556-024-01511-x.

Correspondence and requests for materials should be addressed to Bianxiao Cui.

Peer review information *Nature Cell Biology* thanks Johann Böhm, Vincenzo Sorrentino and the other, anonymous, reviewer(s) for their contribution to the peer review of this work. Peer reviewer reports are available.

https://doi.org/10.1038/s41556-024-01511-x

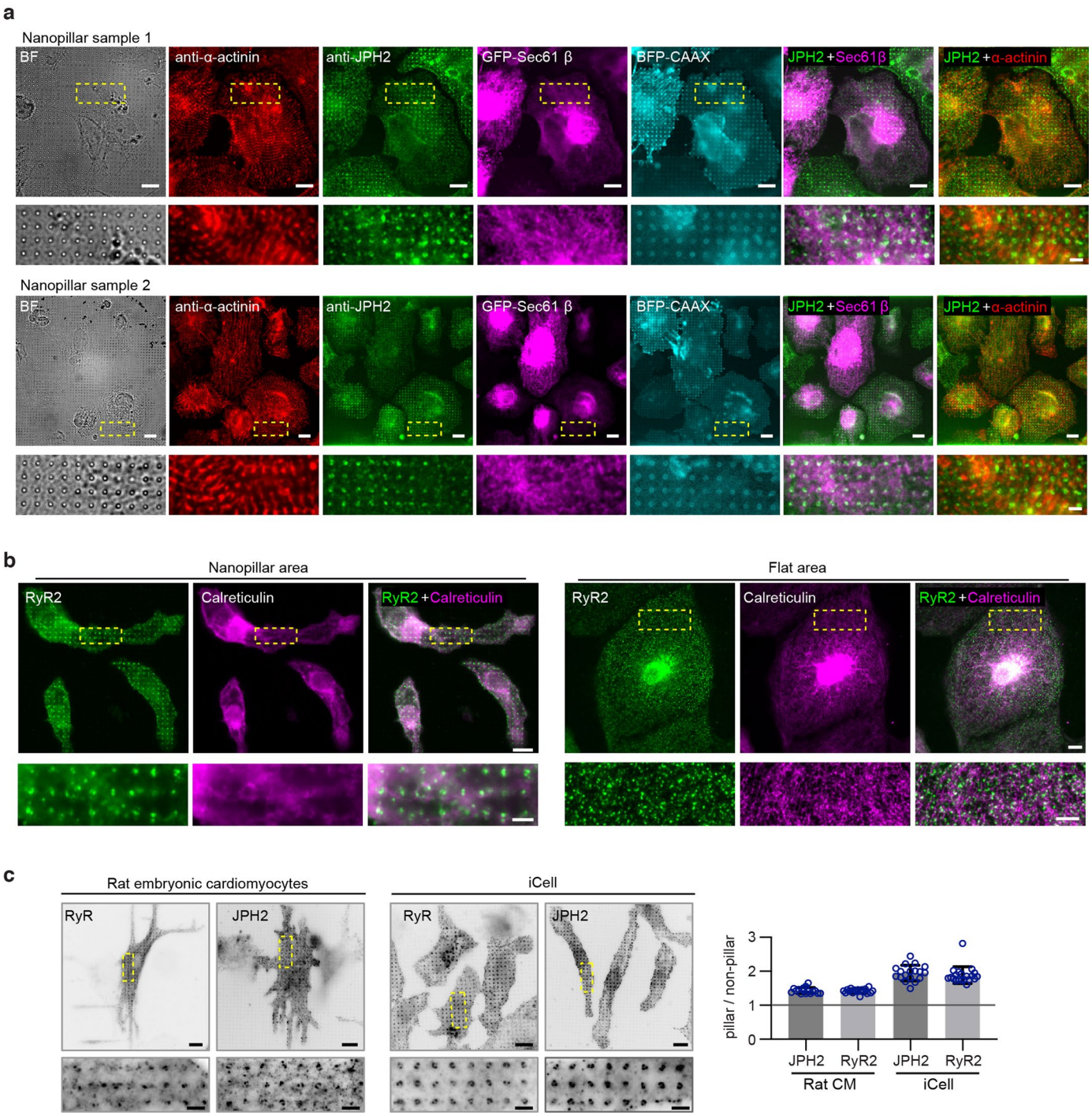

Extended Data Fig. 1 | Nanopillar-induced membrane invaginations recruit dyad components in cardiomyocytes. a, Two additional sets of representative images of co-Immunostained JPH2 (green) and α-actinin (red) in iPSC-CMs expressing GFP-Sec61β (magenta) and BFP-CAAX (cyan) on nanopillars. The experimental condition is the same as in Fig. 1d. **b**, Co-Immunostained RyR2 (green) and Calreticulin (magenta) in iPSC-CMs on nanopillar area (left) and on flat area (right). Magnified images of the yellow boxes are shown at the bottom. **c**, Immunostaining of RyR2 or JPH2 in rat embryonic CMs (left) and iCells (right). Rat embryonic CMs were dissected from E18 rat embryos, plated on nanopillars right after dissection, and cultured for 7 days before fixation and staining. iCells are human iPSC derived CMs from a commercial source (Fujifilm Cellular Dynamics). iCells were seeded on nanopillars and cultured for 51 days before staining. Inverted lookup table is used for clarity. Quantification on the right: the ratio of the fluorescent intensity at the nanopillars over the intensity in between the nanopillars quantified the same way as in Fig. 1g. n = 16, 17, 18, 20 cells for each conditions from left to right. Data are presented as mean values +/− SD. Scale bar 10 μm in top whole cell images, 2.5 μm in bottom zoom-in images for (**a**,**b**,**c**). Experiments in (**c**) were independently replicated two times with similar results, and other experiments were independently replicated three times with similar results. Source numerical data are available in source data Source data.

https://doi.org/10.1038/s41556-024-01511-x

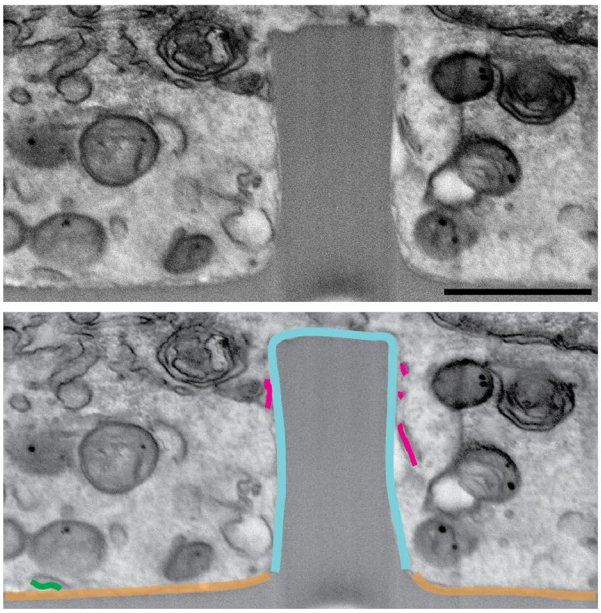

Out of all 36 frames:

$$\text{Pillar ER-PM\%} = \frac{\text{length of ER-PM on pillar}}{\text{length of PM on pillar}} = 12.7\%$$

$$\text{Flat ER-PM\%} = \frac{\text{length of ER-PM on flat}}{\text{length of PM on flat}} = 3.5\%$$

Extended Data Fig. 2 | Illustration of the method to quantify the ER-PM contact overage in FIB-SEM images. One section of the FIB-SEM images shown in Fig. 2c is shown as an example. Upper image is the original image, and the lower image is the same image with the Length of the ER-PM contact on pillar (magenta), the ER-PM contact on the flat (green), the total length of membrane on the pillar (cyan), and the total length of membrane on the flat (orange) color-highlighted. Data from 36 distinct frames were manually collected and the ER-PM contact coverage on nanopillar area and on flat area were then calculated respectively as indicated on the right. Scale bar 100 nm. The experiment was independently replicated two times with similar results.

https://doi.org/10.1038/s41556-024-01511-x

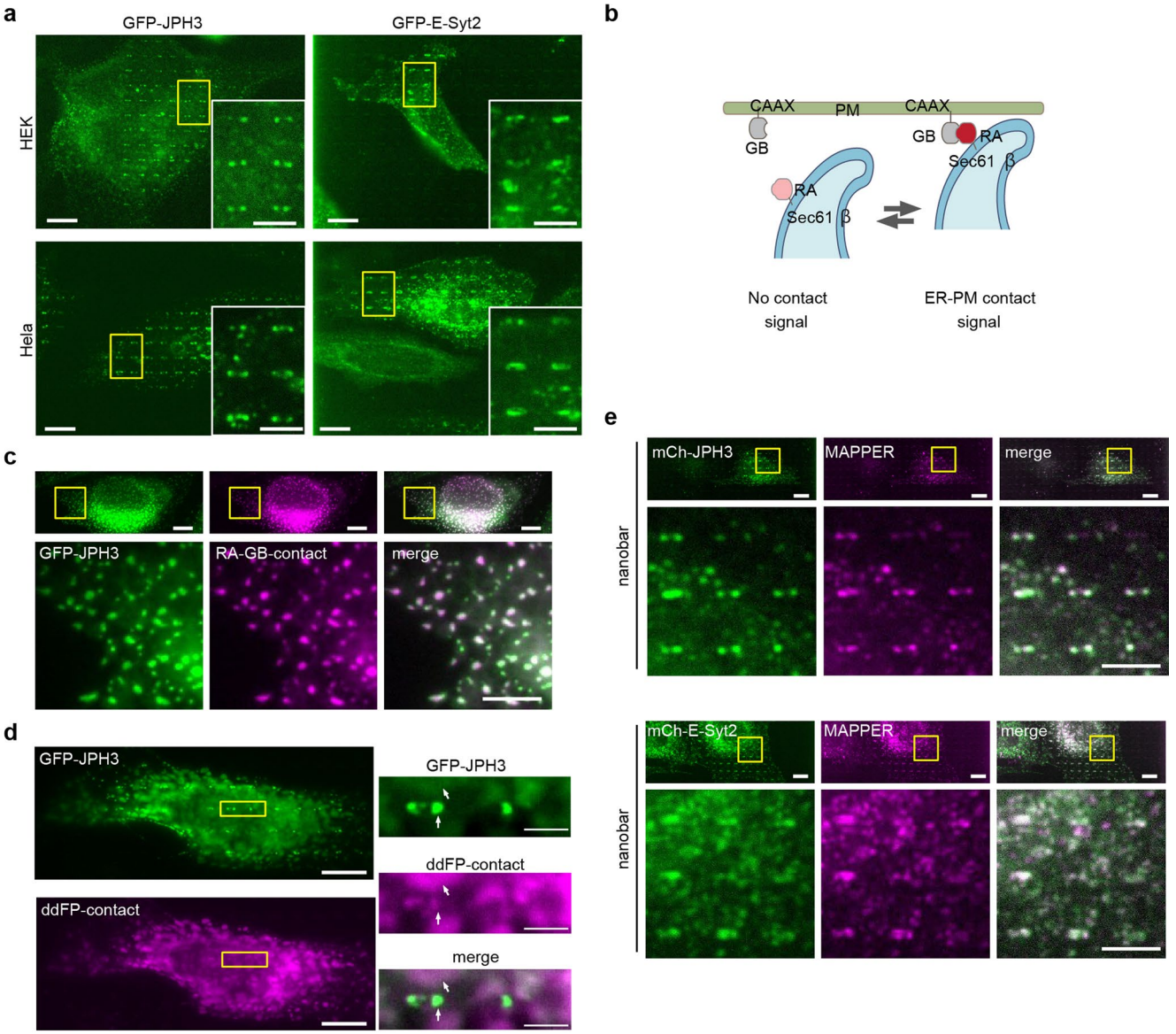

Extended Data Fig. 3 | Distinct spatial distribution of JPH3 and E-Syt2. **a**, Representative images of GFP-JPH3 and GFP-E-Syt2 expressed HEK-297T cells and Hela cells. The quantifications are included in Fig. 3h. Insets show the enlarged 6-nanbar regions in yellow boxes. **b**, A schematic illustration of the ddFP-based ER-PM contact sensor. **c**, ddFP-based ER-PM contact sensor (magenta) and co-expressed GFP-JPH3 (left, green) show extensive colocalization in U2OS cells cultured on flat surfaces. Regions in the yellow boxes are enlarged in the bottom row. **d**, On nanobars, GFP-JPH3 shows stronger preference toward nanobar ends than ddFP-based ER-PM contact sensors. Two-bar region in yellow boxes were enlarged on the right. White arrows point to two distinct contact sites at the nanobar end and the flat surface. **e**, Representative images of GFP-MAPPER (magenta) co-expressed with mCherry-JPH3 (top, green) or mCherry-E-Syt2 (bottom, green) on nanobars. Region in the yellow boxes are enlarged in the bottom row. Scale bar 10 μm in whole cell images, 5 μm in zoom-in images for (**a**,**c**,**e**), 2.5 μm in zoom-in images for (**d**). All experiments were independently replicated three times with similar results.

https://doi.org/10.1038/s41556-024-01511-x

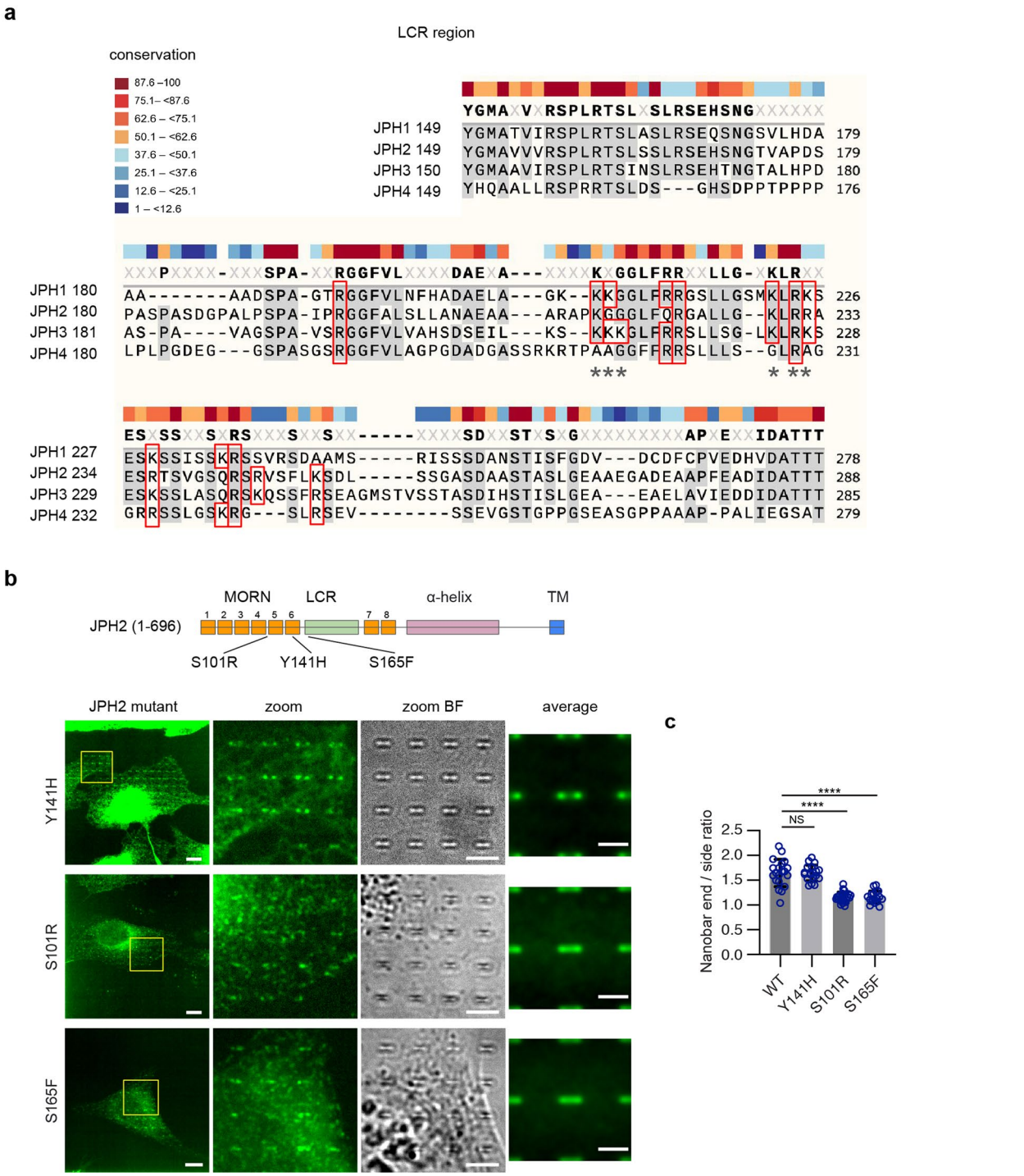

Extended Data Fig. 4 | Conserved polybasic residues in LCR, and hypertrophic cardiomyopathy-associated point mutations in JPH2. a, Alignments are generated from Snapgene. The positively charged residues are contained in the red boxes. Conserved residues and substitutions are colored as indicated. The numbers on the left refer to the position of the first residue shown in each row. The * marked amino acids were mutated into alanine (K210A, K211A, K212A, K224A, R226A, K227A) in the LCR_KRtoA mutant in Fig. 5e. **b**, Representative images of U2OS cells expressing GFP-tagged JPH2 mutants associated with hypertrophic cardiomyopathy. Left: whole cell images; Middle: enlarged fluorescent view and bright field view of the regions in yellow boxes; Right: averaged nanobar images from multiple cells. Cell number: n = 19 (Y141H), 25 (S101R), 18 (S165F). Diagram of the position of each point mutation shown on the top. Scale bar 10 μm (whole cell), 5 μm (zoom), 2.5 μm (average). **c**, Quantifications of the nanobar end-to-side ratios for WT-JPH2, JPH2-Y141H, JPH2-S101R, and JPH2-S165F. Cell number is the same as in (**b**). Data are presented as mean values +/− SD. ****P < 0.0001, NS P > 0.9999. All experiments were independently replicated three times with similar results. One-way Brown-Forsythe and Welch ANOVA tests was used to assess significance for (**c**). Source numerical data are available in source data Source data.

https://doi.org/10.1038/s41556-024-01511-x

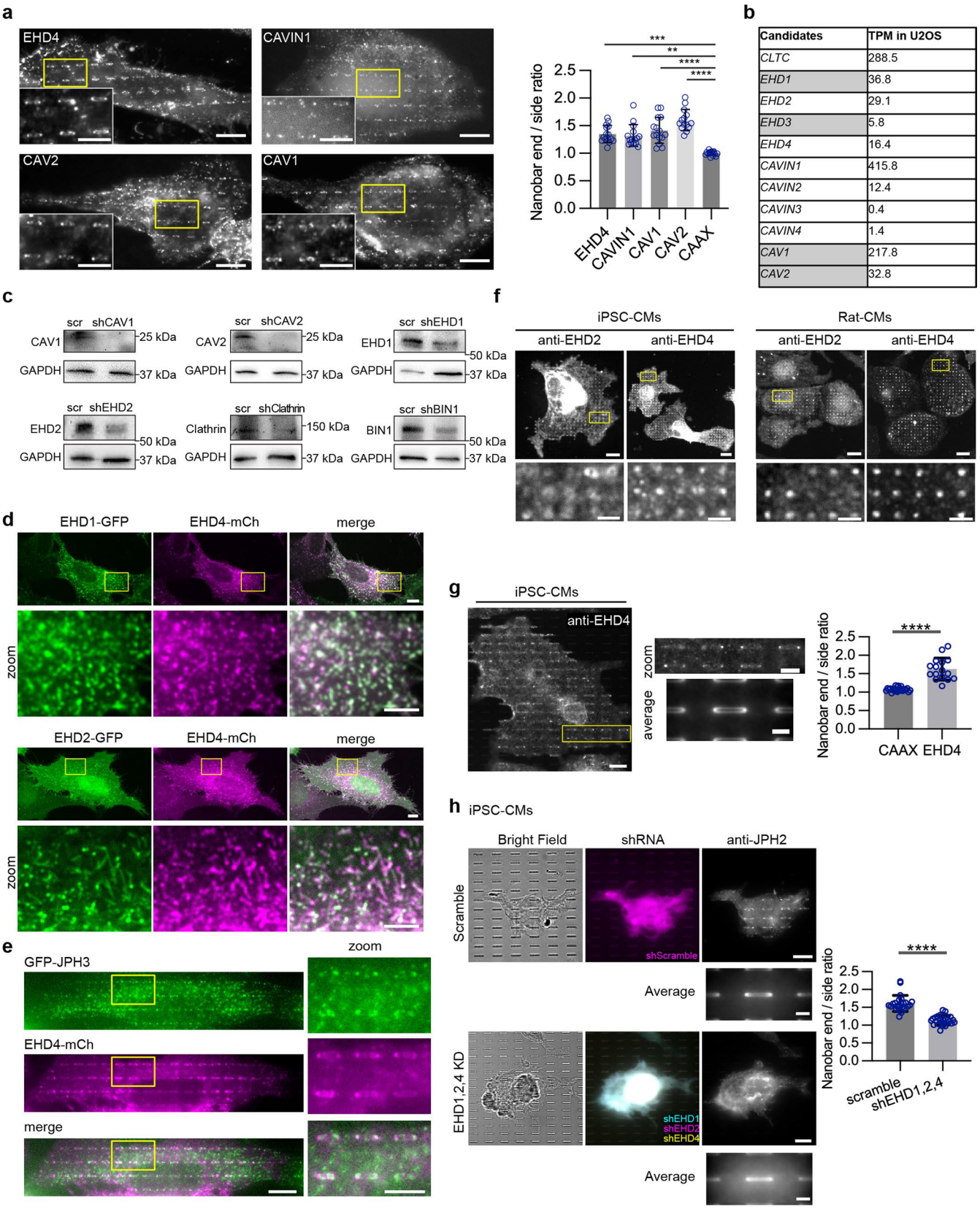

Candidates	TPM in U2OS
CLTC	288.5
EHD1	36.8
EHD2	29.1
EHD3	5.8
EHD4	16.4
CAVIN1	415.8
CAVIN2	12.4
CAVIN3	0.4
CAVIN4	1.4
CAV1	217.8
CAV2	32.8

Extended Data Fig. 5 | See next page for caption.

https://doi.org/10.1038/s41556-024-01511-x

Extended Data Fig. 5 | EHDs sense PM curvatures and play important roles in JPH's membrane curvature targeting. a, EHD4-GFP, GFP-CAVIN1, GFP-CAV1, and GFP-CAV2 in U2OS on nanobars. Right: end-to-side ratios quantification. Cell number: n = 14 (CAV2), n = 15 (all others). ***P = 0.0001, **P = 0.0015; ****P < 0.0001. **b**, Protein transcript levels in U2OS cells (normalized transcripts per million, nTPM). *CLTC* encodes clathrin heavy chain. Genes in gray: not identified in the JPH2 interactome but closely related genetically or functionally. EHD3, CAVIN2, CAVIN3, and CAVIN4 were not knocked down due to low TPM in U2OS cells. **c**, Western blots confirming shRNA knockdown of CAV1, CAV2, EHD1, EHD2, clathrin heavy chain, and BIN1. Glyceraldehyde-3-phosphate dehydrogenase (GAPDH) as a loading control. **d**, Images of U2OS cells co-expressing EHD4-mCherry with EHD1-GFP (Top) or with EHD2-GFP (Bottom). Enlarged views are from yellow boxes. **e**, Images of U2OS cells expressing GFP-JPH3 (green) and EHD4-mCh (magenta) on nanobars. Enlarged views are from yellow boxes. **f**, Images of EHD2 or EHD4 immunostaining in iPSC-CMs or rat embryonic CMs on nanopillars. Bottom: enlarged yellow-box regions. Scale bar: 10 µm (top), 2.5 µm (bottom). **g**, Images of EHD4 immunostaining in iPSC-CMs on nanobars. Middle: enlarged yellow-box regions and averaged fluorescent signals of all nanobars from multiple cells. n = 16 cells. Right: end to side ratios of EHD4 compared to BFP-CAAX expressed in iPSC-CM on nanobars. Cell number: CAAX = 23, EHD4 = 16. ****P < 0.0001. **h**, Images of JPH2 immunostaining in iPSC cells transfected with shRNA of scramble (top) or EHD1/2/4 (bottom). Left to right: Bright field image, fluorescent protein indicating shRNA transfection, and JPH2 staining. Bottom: averaged nanobar images of JPH2 staining from multiple cells. Right: end-to-side ratio. Cell number: Scramble = 24, shEHD1/2/4 = 26. ****P < 0.0001. Scale bars: 10 µm (whole cell), 5 µm (enlarged region), 2.5 µm (average), unless otherwise mentioned. Experiments in (**h**) were independently replicated two times with similar results, and others were independently replicated for three times with similar results. Data are mean values +/− SD for (**a,g,h**). Kruskal–Wallis test corrected with Dunn's multiple-comparison test was used to assess significance in (**a**). Unpaired two-tailed Welch's t test was used in (**g**). Two-tailed Mann-Whitney test was used in (**h**). Source numerical data and unprocessed blots are available in source data Source data.

https://doi.org/10.1038/s41556-024-01511-x

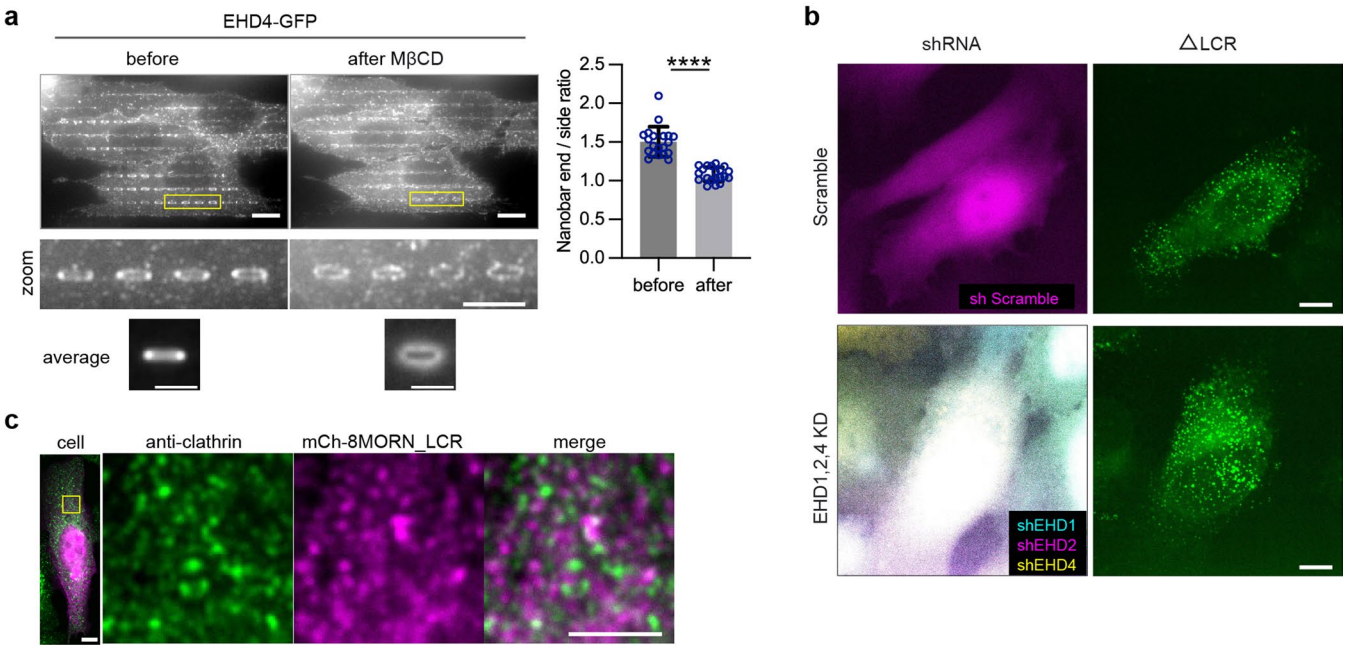

Extended Data Fig. 6 | EHD4's PM curvature sensitivity is cholesterol dependent, MORN motifs possess PM affinity and MORN_LCR interacts with EHD4. a, The distribution of EHD4-GFP on nanobars before and after 10 mM MβCD treatment at 37 °C for 30 min. Magnified images of the yellow boxes are shown in the middle row. Averaged fluorescent signals of all nanobars from multiple cells were averaged and displayed in the bottom row. Quantifications of the end-to-side ratios are shown on the right. n = 15 cells for both conditions. Data are presented as mean values +/− SD. ****P < 0.0001. **b**, Representative images of GFP-ΔLCR expressed in EHD-1,−2,−4 triple knockdown U2OS cells (bottom) or scramble knockdown control U2OS cells (top). **c**, Representative images of U2OS cells expressing mCherry-8MORN_LCR (magenta) and immunostained with clathrin-heavy-chain antibody (green). Enlarged views are zoomed from the yellow boxes in whole cell images. Quantification of this data was shown in Fig. 6h. Scale bar 10 μm (whole cell), 5 μm (enlarged image), 2.5 μm (average). Experiments in (**b**) were independently replicated two times with similar results, and other experiments were independently replicated three times with similar results. Unpaired two-tailed Welch's t test was used to assess the significance in (**a**). Source numerical data are available in source data Source data.

https://doi.org/10.1038/s41556-024-01511-x

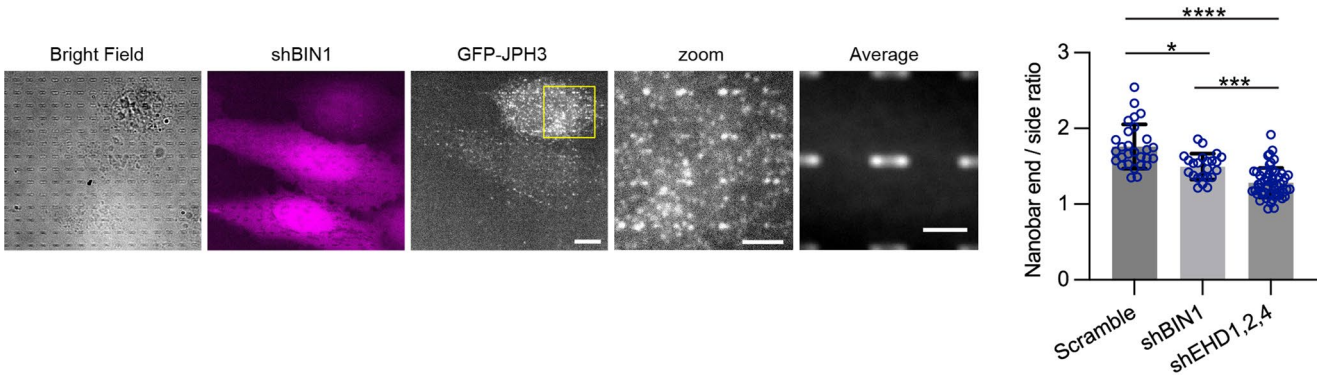

Extended Data Fig. 7 | BIN1 knockdown mildly reduces the curvature preference of JPH3. Representative images of GFP-JPH3 in U2OS expressing a BIN1 shRNA. Bright field and the fluorescent protein co-expressed with shRNA are shown on the left. Zoom is the enlarged view of the region in yellow box. Averaged image of all nanobars from multiple cells is shown on the right. Cell number for average: Scramble = 28; shBIN1 = 23; shEHD1,2,4 = 55. Scale bars all 10 µm (whole cell), 5 µm (enlarged image), 2.5 µm (average). Quantification on the right shows the end-to-side ratios of GFP-JPH3 in BIN1 KD cells compared to those in scramble control and EHD1,2,4 KD cells. The experiment was independently replicated for three times with similar results. Data are presented as mean values +/− SD. Kruskal–Wallis test corrected with Dunn's multiple-comparison test was used to assess significance. *P = 0.0382, ***P = 0.0008, ****P < 0.0001. Source numerical data are available in source data Source data.

nature portfolio

Corresponding author(s): Bianxiao Cui

Last updated by author(s): Aug 1, 2024

Reporting Summary

Nature Portfolio wishes to improve the reproducibility of the work that we publish. This form provides structure for consistency and transparency in reporting. For further information on Nature Portfolio policies, see our Editorial Policies and the Editorial Policy Checklist.

Statistics

For all statistical analyses, confirm that the following items are present in the figure legend, table legend, main text, or Methods section.

n/a	Confirmed
☐	☒ The exact sample size (*n*) for each experimental group/condition, given as a discrete number and unit of measurement
☐	☒ A statement on whether measurements were taken from distinct samples or whether the same sample was measured repeatedly
☐	☒ The statistical test(s) used AND whether they are one- or two-sided *Only common tests should be described solely by name; describe more complex techniques in the Methods section.*
☐	☒ A description of all covariates tested
☐	☒ A description of any assumptions or corrections, such as tests of normality and adjustment for multiple comparisons
☐	☒ A full description of the statistical parameters including central tendency (e.g. means) or other basic estimates (e.g. regression coefficient) AND variation (e.g. standard deviation) or associated estimates of uncertainty (e.g. confidence intervals)
☐	☒ For null hypothesis testing, the test statistic (e.g. *F*, *t*, *r*) with confidence intervals, effect sizes, degrees of freedom and *P* value noted *Give P values as exact values whenever suitable.*
☒	☐ For Bayesian analysis, information on the choice of priors and Markov chain Monte Carlo settings
☒	☐ For hierarchical and complex designs, identification of the appropriate level for tests and full reporting of outcomes
☐	☒ Estimates of effect sizes (e.g. Cohen's *d*, Pearson's *r*), indicating how they were calculated

Our web collection on statistics for biologists contains articles on many of the points above.

Software and code

Policy information about availability of computer code

Data collection	Leica LAS X, Nikon NIS-Elements AR
Data analysis	MATLAB 2023a (MathWorks), ImageJ (Fiji 2.13), Prism 9.5.1 (GraphPad software). Custom MATLAB codes were published in previous research by our lab (Zhang, W. et al. Nat. Cell Biol.25, 1453–1464 (2023)) and are available on github (Link: github.com/wzhang5publication/Data-analysis).

For manuscripts utilizing custom algorithms or software that are central to the research but not yet described in published literature, software must be made available to editors and reviewers. We strongly encourage code deposition in a community repository (e.g. GitHub). See the Nature Portfolio guidelines for submitting code & software for further information.

Data

Policy information about availability of data

All manuscripts must include a data availability statement. This statement should provide the following information, where applicable:

- Accession codes, unique identifiers, or web links for publicly available datasets
- A description of any restrictions on data availability
- For clinical datasets or third party data, please ensure that the statement adheres to our policy

Source data have been provided in Source Data. Referenced dataset of JPH2 bio interactome is from Mass Spectrometry Interactive Virtual Environment:

MSV00008435247, and referenced protein atlas is from https://www.proteinatlas.org. All other data supporting the findings of this study are available from the corresponding author on reasonable request.

Research involving human participants, their data, or biological material

Policy information about studies with human participants or human data. See also policy information about sex, gender (identity/presentation), and sexual orientation and race, ethnicity and racism.

Reporting on sex and gender	N/A
Reporting on race, ethnicity, or other socially relevant groupings	N/A
Population characteristics	N/A
Recruitment	N/A
Ethics oversight	N/A

Note that full information on the approval of the study protocol must also be provided in the manuscript.

Field-specific reporting

Please select the one below that is the best fit for your research. If you are not sure, read the appropriate sections before making your selection.

☒ Life sciences ☐ Behavioural & social sciences ☐ Ecological, evolutionary & environmental sciences

For a reference copy of the document with all sections, see nature.com/documents/nr-reporting-summary-flat.pdf

Life sciences study design

All studies must disclose on these points even when the disclosure is negative.

Sample size	No sample size calculation was performed. Sample size was determined based on our previous experimental experience (e.g., Zhang, W. et al. Nat. Cell Biol.25, 1453–1464 (2023); Zhao, W. et al. Nat. Nanotechnol. 12, 750–756 (2017); Lou, H.-Y. et al. PNAS 116, 23143–23151 (2019)). Similar sample sizes have been used in many recent papers from other labs, such as Shiu, J.-Y. et al. Nat. Cell Biol. 20, 262–271 (2018); Changede, R. et al. Nat. Mater. 18, 1366–1375 (2019); Oria, R. et al. Nature 552, 219–224 (2017).
Data exclusions	No data were excluded for data analysis.
Replication	All experiments were repeated independently at least two times with similar results.
Randomization	The experiments were not randomized. This is not applicable in our research since we mostly work with cell lines, which is considered homogeneous or random already.
Blinding	Blinding was not performed, as the protein sub-cellular distribution would clearly reveal the sample identity to investigators during most experiments. All data were collected automatically by instruments other than by human evaluation.

Reporting for specific materials, systems and methods

We require information from authors about some types of materials, experimental systems and methods used in many studies. Here, indicate whether each material, system or method listed is relevant to your study. If you are not sure if a list item applies to your research, read the appropriate section before selecting a response.

Materials & experimental systems

n/a	Involved in the study
☐	☒ Antibodies
☐	☒ Eukaryotic cell lines
☒	☐ Palaeontology and archaeology
☐	☒ Animals and other organisms
☒	☐ Clinical data
☒	☐ Dual use research of concern
☒	☐ Plants

Methods

n/a	Involved in the study
☒	☐ ChIP-seq
☒	☐ Flow cytometry
☒	☐ MRI-based neuroimaging

Antibodies

Antibodies used

1. anti-junctophilin2 antibody (HPA052646), Sigma, 1:300 dilution for immunofluorescence (IF)
2. anti-α-actinin antibody (A7811), Sigma, 1:1000 dilution for IF
3. anti-Cav1.2 antibody (C1103), Sigma, 1:300 dilution for IF
4. anti-RyR2 antibody (NB1202827), Novus Bio, 1:500 dilution for IF
5. anti-caveolin1 antibody (sc-70516), Santa Cruz, 1:1000 for western blotting (WB)
6. anti-caveolin2 antibody (CSB-PA004572LA01HU-20UG), Cusabio, 1:1000 for WB
7. anti-EHD1 antibody (CSB-PA884470LA01HU-20UG), Cusabio, 1:1000 for WB
8. anti-EHD2 antibody (CSB-PA873710LA01HU-20UG), Cusabio,1:1000 for WB, 1:300 for IF
9. anti-clathrin monoclonal antibody X22 (MA1-065), Invitrogen, 1:1000 for WB
10. anti-GFP antibody (A-11122), Invitrogen, 1:1000 for WB
11. HRP-linked goat anti-rabbit IgG (H+L) antibody (7074), Cell Signaling Technology, 1:1000 for WB
12. HRP-linked goat anti-mouse IgG (H+L) antibody (7076), Cell Signaling Technology, 1:1000 for WB
13. anti-mCherry antibody (SAB2702291), Sigma, 1:1000 for WB
14. anti-BIN1 antibody (SAB1408547), Sigma, 1:1000 for WB
15. anti-EHD4 antibody (50-172-7111), Fisher Scientific, 1:400 for IF
16. anti-Calreticulin antibody (PA3-900), Invitrogen,1:400 for IF
17. Alexa FluorTM 594-goat anti-rabbit IgG, Invitrogen, 1:1000 for IF
18. Alexa FluorTM647-goat anti-mouse IgG, Invitrogen, 1:1000 for IF

Validation

The antibodies have been validated by the manufacturers and previous publications.
Details are available from the references below.
1. anti-junctophilin2 antibody: https://www.sigmaaldrich.com/US/en/product/sigma/hpa052646
2. anti-α-actinin antibody: https://www.sigmaaldrich.com/US/en/product/sigma/a7811
3. anti-Cav1.2 antibody: https://www.sigmaaldrich.com/US/en/product/sigma/c1103
4. anti-RyR2 antibody: https://www.novusbio.com/products/ryanodine-receptor-1-antibody-c3-33_nb120-2827
5. anti-caveolin1 antibody: https://www.scbt.com/p/caveolin-1-antibody-4h312
6. anti-caveolin2 antibody: https://www.cusabio.com/Polyclonal-Antibody/CAV2-Antibody-12551400.html
7. anti-EHD1 antibody: https://www.cusabio.com/Polyclonal-Antibody/EHD1-Antibody-12259683.html
8. anti-EHD2 antibody: https://www.cusabio.com/Polyclonal-Antibody/EHD2-Antibody-12549425.html
9. anti-clathrin monoclonal antibody X22: https://www.thermofisher.com/antibody/product/Clathrin-Heavy-Chain-Antibody-clone-X22-Monoclonal/MA1-065
10. anti-GFP antibody: https://www.thermofisher.com/antibody/product/GFP-Antibody-Polyclonal/A-11122
11. HRP-linked goat anti-rabbit IgG (H+L) antibody: https://www.cellsignal.com/products/secondary-antibodies/anti-rabbit-igg-hrp-linked-antibody/7074
12. HRP-linked goat anti-mouse IgG (H+L) antibody: https://www.cellsignal.com/products/secondary-antibodies/anti-mouse-igg-hrp-linked-antibody/7076
13. anti-mCherry antibody: https://www.sigmaaldrich.com/US/en/product/sigma/sab2702291
14. anti-BIN1 antibody: https://www.sigmaaldrich.com/US/en/product/sigma/sab1408547
15. anti-EHD4 antibody: https://www.fishersci.com/shop/products/ehd4-rabbit-anti-human-mouse-rat-polyclonal-proteintech-2/501727111?emb_id=pp_usbackorderupdate_producttitle
16. anti-Calreticulin antibody: https://www.thermofisher.com/antibody/product/Calreticulin-Antibody-Polyclonal/PA3-900
17.Alexa FluorTM 594-goat anti-rabbit IgG: https://www.thermofisher.com/antibody/product/Goat-anti-Rabbit-IgG-H-L-Cross-Adsorbed-Secondary-Antibody-Polyclonal/A-11012
18.Alexa FluorTM647-goat anti-mouse IgG: https://www.thermofisher.com/antibody/product/Goat-anti-Mouse-IgG-H-L-Highly-Cross-Adsorbed-Secondary-Antibody-Polyclonal/A32728

Eukaryotic cell lines

Policy information about cell lines and Sex and Gender in Research

Cell line source(s)

U2OS (ATCC HTB-96™), HeLa (ATCC CCL-2™), HEK293T cells (ATCC® CRL-3216™), iCells (Fujifilm Cellular Dynamics, 01434), HL-1 cells (laboratory of William C. Claycomb at Louisiana State University, available from Millipore SCC065).

Authentication

Cell line authentication was not performed. All cell lines were expanded from the original vials vendors provided and used for experiments within twenty passages.

Mycoplasma contamination

All cell lines were tested negative for mycoplasma contamination by RT-PCR.

Commonly misidentified lines
(See ICLAC register)

We did not use commonly misidentified lines listed by ICLIAC.

Animals and other research organisms

Policy information about studies involving animals; ARRIVE guidelines recommended for reporting animal research, and Sex and Gender in Research

Laboratory animals

Sprague Dawley rat embryos used in this study were in embryonic day 18 from Charles River Laboratories.

Wild animals

No wild animals were used in this study

Reporting on sex	We did not examine the sex because we assumed the embryonic cardiomyocytes behave similarly in the scope of our study.
Field-collected samples	No Field-collected samples were used in this study
Ethics oversight	iPSCs were obtained from Stanford Cardiovascular Institute Biobank and used per IRB/SCRO Panel guidelines, which adheres to federal, state and Stanford human stem cell research policies. Use of laboratory rats was approved by the Stanford University administrative panel on laboratory animal care, and adhered to relevant ethical regulations.

Note that full information on the approval of the study protocol must also be provided in the manuscript.

Plants

Seed stocks	*Report on the source of all seed stocks or other plant material used. If applicable, state the seed stock centre and catalogue number. If plant specimens were collected from the field, describe the collection location, date and sampling procedures.*
Novel plant genotypes	*Describe the methods by which all novel plant genotypes were produced. This includes those generated by transgenic approaches, gene editing, chemical/radiation-based mutagenesis and hybridization. For transgenic lines, describe the transformation method, the number of independent lines analyzed and the generation upon which experiments were performed. For gene-edited lines, describe the editor used, the endogenous sequence targeted for editing, the targeting guide RNA sequence (if applicable) and how the editor was applied.*
Authentication	*Describe any authentication procedures for each seed stock used or novel genotype generated. Describe any experiments used to assess the effect of a mutation and, where applicable, how potential secondary effects (e.g. second site T-DNA insertions, mosiacism, off-target gene editing) were examined.*